

# A Comprehensive Review of Markov Random Field and Conditional Random Field Approaches in Pathology Image Analysis

Yixin Li · Chen Li (Corresponding author) · Xiaoyan Li (Corresponding author) · Kai Wang · Md Mamunur Rahaman · Changhao Sun · Hao Chen · Xinran Wu · Hong Zhang · Qian Wang

Received: date / Accepted: date

Yixin Li  
 Microscopic Image and Medical Image Analysis Group, MBIE College, Northeastern University, Shenyang, China  
 E-mail: 1047792668@qq.com

Chen Li  
 Microscopic Image and Medical Image Analysis Group, MBIE College, Northeastern University, Shenyang, China  
 E-mail: lichen201096@hotmail.com

Xiaoyan Li  
 Cancer Hospital of China Medical University, Shengyan, China  
 E-mail: lixiaoyan@cancerhosp-ln-cmu.com

Kai Wang  
 Shenyang Institute of Automation, Chinese Academy of Sciences, Shenyang, China  
 E-mail: wangkai@sia.cn

Md Mamunur Rahaman  
 Microscopic Image and Medical Image Analysis Group, MBIE College, Northeastern University, Shenyang, China  
 E-mail: mamunrobi35@gmail.com

Changhao Sun  
 Microscopic Image and Medical Image Analysis Group, MBIE College, Northeastern University, Shenyang, China  
 E-mail: sch236@sina.com

Hao Chen  
 School of Nanjing University of Science and Technology, Nanjing, China  
 E-mail: 451091574@qq.com

Xinran Wu  
 Microscopic Image and Medical Image Analysis Group, MBIE College, Northeastern University, Shenyang, China  
 E-mail: 975990071@qq.com

Hong Zhang  
 Shengjing Hospital of China Medical University, Shenyang, China  
 E-mail: haojiubujian1203@sina.cn

Qian Wang  
 Cancer Hospital of China Medical University, Shengyan, China

**Abstract** Pathology image analysis is an essential procedure for clinical diagnosis of numerous diseases. To boost the accuracy and objectivity of the diagnosis, nowadays, an increasing number of intelligent systems are proposed. Among these methods, random field models play an indispensable role in improving the investigation performance. In this review, we present a comprehensive overview of pathology image analysis based on the *Markov Random Fields* (MRFs) and *Conditional Random Fields* (CRFs), which are two popular random field models. First of all, we introduce the framework of two random field models along with pathology images. Secondly, we summarize their analytical operation principle and optimization methods. Then, a thorough review of the recent articles based on MRFs and CRFs in the field of pathology is presented. Finally, we investigate the most commonly used methodologies from the related works and discuss the method migration in computer vision.

**Keywords** Markov random fields · Conditional random fields · Pathology image analysis · Image classification · Image segmentation

## 1 Introduction

### 1.1 Markov Random Fields

*Markov Random Fields* (MRFs), one of the classical undirected *Probabilistic Graphical Models*, belongs to the Bayesian framework [1]. Each object of the MRFs, which is called a ‘node’ (or vertex or point) in the graphical models, denotes a random variable and connected

China  
 E-mail: wangqian\_an\_16@163.com

by an ‘edge’ between them. In image analysis domain, the MRFs can describe the pixel-spatial interaction due to its structure and thus is developed initially to analyze the spatial relationship of physical phenomena. However, the number of possible states of MRFs is excessively broad, and its joint distribution is hard to be calculated [2].

In 1971, Hammersley and Clifford proved the equivalence between the MRFs and Gibbs distribution and this theory is lately developed by [3]. An explicit and elegant formula models the joint distribution of MRF due to the MRFs-Gibbs equivalence, where the probability is described by a potential function [4]. The proposed optimization algorithms such as Iterative Condition Mode (ICM) and Expectation Maximization (EM) and MRFs-Gibbs equivalence make the MRFs a practical model. Additionally, as mentioned above, the MRF model considers the important spatial constraint, which is essential to interpret the visual information. Hence, the MRFs have attracted significant attention from scholars since it is proposed.

The very first research performed to segment medical images using MRFs are in [5]. After persistent and in-depth research in last two decades, the MRFs are now widely adopted to solve problems in computer vision, consisting of image reconstruction, image segmentation as well as image classification [6]. However, MRFs also have limitations: the joint probability of the images and its annotations are modelled due to the underlying generative nature of MRFs, resulting in a complicated structure that requires a large amount of computation. The high difficulty of parameter estimation due to the huge amount of parameters based on the MRF becomes the bottleneck of its growth [7].

## 1.2 Conditional Random Fields

*Conditional Random Fields* (CRFs), as an important and prevalent type of machine learning method, is constructed for data labeling and segmentation. Contrary to generative nature of MRF, it is an undirected discriminative graphical model focusing on the posterior distribution of observation and possible label sequence [8]. Developed based on the Maximum Entropy Markov Models (MEMMs) [9], the CRFs avoid the fundamental limitations and of it and other directed graphical models like Hidden Markov Model (HMM) [10].

Compared to the Bayesian models proposed before, the CRF models have three main advantages: First, the CRF models solve the label bias problem of MEMMs, which is the main deficiency. Second, the CRFs models the probability of a label sequence for a known

observation array, which is called condition probability. Compared to other generative models whose usual training goal for the parameters is the joint probability function maximization. In contrast, the CRF models are not required to traverse all possible observation sequences, which is typically intractable. Thirdly, the CRFs relax the strong dependencies assumption in other Bayesian models based on directed graphical models and are capable of building higher-order dependencies, which means that the results of CRFs are more closer to the true distribution of the data. The CRF models have many different variants, such as Fully-connected CRF (FC-CRF) and deep Gaussian CRF. The Maximum A Posteriori Estimation (MAP) method is usually utilized for unknown parameters inference of the CRFs [11].

The CRFs attract researchers’ interest in the domain of machine learning because various application scenarios can apply CRFs achieving better results, such as for Name Entity Recognition Problem in Natural Language Processing [12], Information Mining [13], Behavior Analysis [14], Image and Computer Vision [15], and Biomedicine [16]. In recent year, with the rapid development of deep learning (DL), the CRF models are usually utilized as an essential pipeline within the deep neural network in order to refine the image segmentation results [7]. Some researches [14] incorporate them into the network architecture, while others [17] include them into the post-processing step. Studies show that they mostly achieve better performances than before.

## 1.3 Pathology Image Analysis

The term ‘pathology’ has different meanings under different conditions. It usually refers to histopathology and cytopathology, and under other circumstances, it refers to other subdiscipline. To avoid confusion, the term ‘pathology’ refers to histopathology and cytopathology in this paper, which detect morphological changes of a lesion like tissue and cellular structure under a microscope. For purpose of obtaining a tumor sample, performing a biopsy or aspiration requiring intervention such as an image-guided procedure or endoscopy is a real necessity [18].

Pathology image analysis is considered as one of the key elements of early diagnosis of various diseases, especially cancer, reported by the World Health Organization (WHO) [19]. Cancer is now responsible for nearly 16.7% death in the world, and over 14 million people are diagnosed as cancer every year. It is found that the ability to provide screening and early cancer diagnosis has a significant impact on improving the curing rate, reducing mortality over cancer and cutting treatment

costs, because the main problem now is that numerous cancer cases are already at an advanced stage when they are diagnosed [20]. An accurate pathologic diagnosis is critical, and the reasons are as follows: First, the definitive diagnosis of cancer and other diseases like retinopathy must be made by morphological and phenotypical examination of suspected lesion. Second, especially for cancer, pathology image analysis is essential to determine the degree of tumor spread from the original site, which is also called staging. Thirdly, the appropriate treatment afterwards relies on various pathologic parameters, including the type, grade and extent of cancer [18, 21].

Traditionally, pathology results are provided by manual assessment. However, due to the laborious and tedious nature of pathologists' work as well as the complexity and heterogeneity, the manual analysis is relatively subjective and even leads to misdiagnosis [22]. With the rapid advance of technology, Computer-Aided Diagnosis (CAD) emerges, which promises hopefully more standardized and objective diagnosis comparing to manual inspection. Besides, CAD can offer quantitative result. In the preceding decades, there have been numerous researches in CAD area, proposing various algorithms combining prior knowledge and training data in order to help pathologists make clinical diagnosis and researchers in studying disease mechanisms [23].

#### 1.4 Paper Searching and Screening

To collect the papers related to our research interest, we carry out a series of paper searching and screening with Google Scholar's help. The whole process is presented in Fig. 1. During the first round of paper searching, the keyword is applied for a wide range of searches, and a total of 188 papers are found. After carefully reading the abstract, 141 papers related to the imaging principle or other imaging methods are precluded. And 47 papers are retained, including 28 papers related to microscopic image analysis, 11 papers related to micro-alike images analysis, and ten review papers. Afterward, the second research mainly focuses on the reference in the above 47 papers and the review, and 16 papers are selected from a large number of citations. Finally, 59 research papers remain and to be concluded in our review.

#### 1.5 Motivation of This Review

Pathology image analysis influences disease detection in a significant way. However, manual detection of microscopic images requires exhaustive examination and

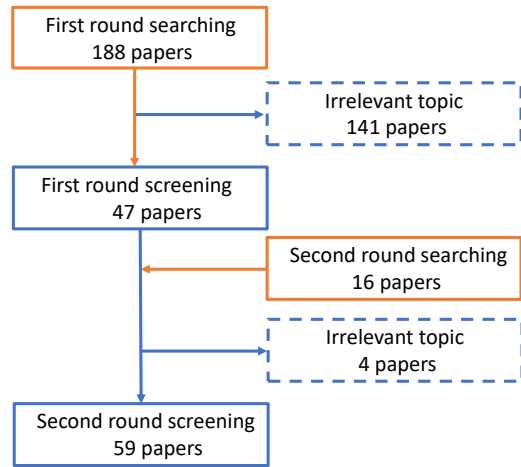


**Fig. 1** The flowchart of the paper searching and screening process.

analysis by a small number of experienced pathologists, and the detection results may be subjective and vary from different pathologists. Especially for Whole-slide Images (WSIs), which are extensively large (e.g.,  $100,000 \times 200,000$  pixels), it is labor-intensive and time-consuming to achieve fine-grained results [24]. Therefore, various intelligent diagnosis systems are introduced to assist pathologists in detecting diseases. In this process, image labeling serving as the intermediate step is in a significant position. To some degree, the accuracy of the whole process is associated with the quality of the image labeling. In terms of labeling, each pixel's label is not only related to its individual information but also depends on its neighborhood [7]. For instance, a WSI is divided into small patches, when a patch is labeled as a tumor, there is a probability that its neighbouring patches are also labeled as tumor [24]. Moreover, researches are suggesting that the distribution of labels in pathology images has a specific underlying structure proved to be beneficial to diagnosis [25]. However, some existing methods do not take the contextual information on neighboring labels into consideration. For example, some traditional binary classifiers like Support Vector Machine (SVM) and Maximum Entropy only consider one single input and ignore the spatial relationship with other inputs while predicting the labels [8]. Besides, the advanced DL models also have this problem. Although the Convolutional Neural Network (CNN) has a large number of input images, the spatial dependencies on patches are usually neglected, and the inference is only based on the appearance of individual patches [26]. Hence, the structural model is proposed to solve this problem. The most prevalent models are the MRFs and the CRFs, which explicitly model

the correlation of the pixels or the patches being predicted [27]. A better result can be obtained if the information from the neighbouring patches are integrated into the MRFs or the CRFs. Therefore, by incorporating them into the CNNs, the small spurious regions like noisy isolated predictions in the original output are almost eliminated [28]. Meanwhile, the boundaries are proved to be refined and become smoother [29].

According to our survey, a limited number of reviews concentrate on medical image analysis and random fields. Among these studies, [8] focuses on the CRFs and their application for different area. Some surveys [7, 30] concentrate on image analysis with random field models. However, those papers rarely refer to medical image analysis, let alone pathology image analysis. Additional papers direct on Artificial Intelligence in pathology image analysis [31, 32], such as using the DL algorithm [33–35] and other image analysis techniques [36, 37]. Those papers introduce various algorithms or models, but the literature quantity about random field models is too limited to discuss them specifically, which is inconsistent with their importance. In the following paragraphs, eleven of these reviews are listed and analyzed in detail.

He et al. [36] publishes a research survey in 2012, presenting a summary of CAD techniques in histopathology image analysis domain, aiming at detecting and classifying carcinoma automatically. This paper also introduces the MRFs in a separate paragraph. However, this paper refers to around 158 related works, only including seven papers related to the MRFs or CRFs.

Wang et al. [30] in 2013 provides an overview of MRFs which is applied in computer vision field, and they summarize over 200 papers based on the MRFs. Among them, only seven papers focus on medical images, and no paper is related to pathology image analysis.

Irshad et al. [38] in 2014 summarizes histopathological image analysis methodologies applied in detecting, segmenting and classifying nuclear. According to summarizing table, there are around 100 papers on various image analysis techniques. Among them, there are only two related works using random field models.

Xing et al. [37], in 2016, gives a review concentrating on the newest cell segmentation approaches for microscopy images analysis. In the study, they summarize the CRF models in microscopy image analysis in a separate subsection. This review concludes 326 papers in total, and mainly three papers employ the CRF models for image classification.

Litjens et al. [33] exhibits a review of DL in medical analysis in the year of 2017. This paper provides overviews in a full range of application area, including

neuro, retinal, digital pathology and so on. It summarizes over 300 contributions on various imaging modalities. Among them, twelve papers are relate to random field models.

Chang et al. [31] in 2018 presents a survey article based on recent advances in artificial intelligence applied to pathology. In this paper, around 73 papers associated with this topic are concluded. However, only one paper among them mentions the CRFs.

Wu et al. [7], in 2019, reviews several modern image labeling methods based on the MRFs and CRFs. In addition, they compare the result of random fields with some classical image labeling methods. However, they give less priority of pathology images. Among 28 papers summarized, only one paper concentrates on medical image analysis. No paper is related to pathology images.

Wang et al. [34] publishes a review in 2019, which explores the pathology image segmentation process using DL algorithm. In this review, the detailed process of whole image segmentation is described from data preparation to post-processing step. In the summary survey, there is only one paper based on random field models.

Yu et al. [8], in 2019, publishes a review that presents the summary of different versions of the CRF models and their applications. This paper classifies application fields of the CRFs into four categories, and discusses their application directions in biomedicine separately. There are 37 papers summarized in that subsection. However, only 20 of them concentrate on medical images, and two of them relate to pathology images.

Li et al. [32], in 2020 presents a review that summarizes the recent researches related to cervical histopathology image analysis with machine learning (ML) methods. Various machine learning methods are discussed grouped by the application goals in this research. Only two papers using novel multilayer hidden conditional random fields (MHCRFs) are included.

Rahaman et al. [35], in 2020, gives a review concentrating on cervical cytopathology image analysis. The algorithms applied in the papers concluded are mainly based on DL methods. However, only one research of the 178 papers that focuses on a local FC-CRF combined with the CNNs is described specifically in application in segmentation part.

In addition to the surveys that have mentioned before, there exists other reviews in related fields, such as the works in [4], [39] and [40].

From the existing survey papers, it is evident that many researchers have paid attention to pathology image analysis, or random field models' application. However, we have not found a single review that concentrates on pathological analysis using the MRF and CRF methods. Therefore, this paper gives a comprehensive

review of the relevant work in the past decades. This paper summarizes nearly 40 related works from 2000 to 2019. This is presented in Fig. 2, Fig. 3 and Fig. 4. Fig. 2 illustrates the increasing number of papers that discuss random field models applied in pathology images analysis domain.

From 2002 to 2008, the number of researchers working on the MRFs increased steadily, but the figure remained at a low level. The figure of CRFs stayed zero over that period. After 2002, they all experienced a rapid upward trend. Compared to the papers focusing on the MRFs, that of CRFs grew more rapidly and exceeded its counterpart in 2017. Overall, the total number of research papers saw a consistent rise throughout the period shown.

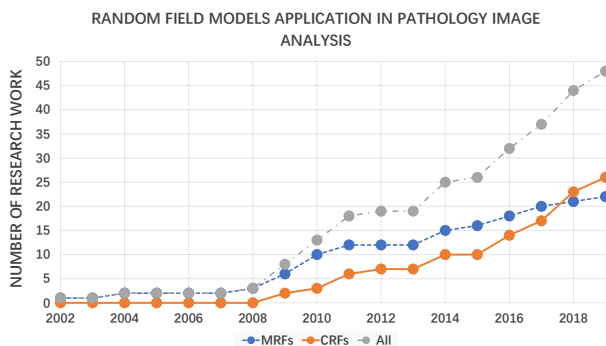


**Fig. 2** Development trend for MRFs and CRFs methods applied in pathology image analysis.

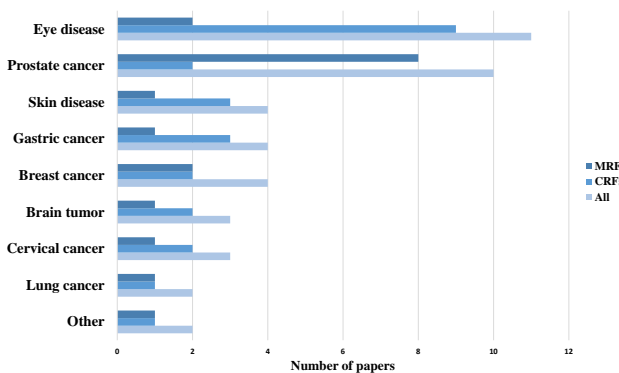


**Fig. 3** Breakdown of the papers included in this survey in year of medical application area.

Concluded from the papers that have been mentioned, a flow chart is given and shown in Fig. 5. It includes the most popular methods in each step that have been used in pathology image analysis.

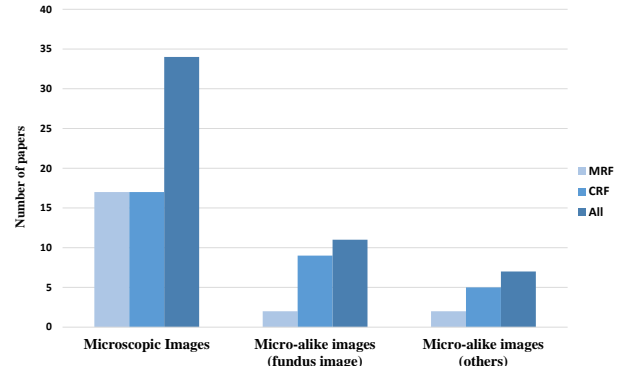


**Fig. 4** Breakdown of the papers included in this survey in year of medical imaging modality.

## 1.6 Data Description

It is observed from the reviewed papers that publicly available retinal datasets are frequently used to prove the effectiveness of the proposed method or make comparisons between different approaches. These datasets are detailed in Table 1.

## 2 Basic Knowledge of MRFs and CRFs

The goal of this section is to provide a formal introduction of the basic knowledge of the MRFs and CRFs, including their modeling process, property and inference. The background of the two models is shown in Fig. 6.

### 2.1 Basic Knowledge of MRFs

#### 2.1.1 Modeling of MRFs

The random field models' key elements contain the node and the edge in the probabilistic graphical model. The key mathematical symbols during modeling process are listed in Table 2. The triplet  $(G, \Omega, P)$  is finally defined as the random field model.

#### 2.1.2 Property of MRFs

If the local conditional probability density functions (LCPDFs) of the random field  $(G, \Omega, P)$  conform to the characteristics of the Markov property shown in Eq. 1, it will be defined as an MRF.

$$P(x_s | \mathbf{x}_{-s}) = P(x_s | \mathbf{x}_{\eta_s}), \quad (1)$$

where  $\mathbf{x}_{-s} = (x_1, \dots, x_{s-1}, x_{s+1}, \dots, x_N)$ ,  $\mathbf{x}_{\eta_s} = (x_{\eta_s(1)}, x_{\eta_s(|\eta_s|)})$ , and  $\eta_i \in S$  is the  $i^{th}$  element of the set  $\eta_s$ . Thus, the forms of the LCPDFs are simplified by Markov property [47].

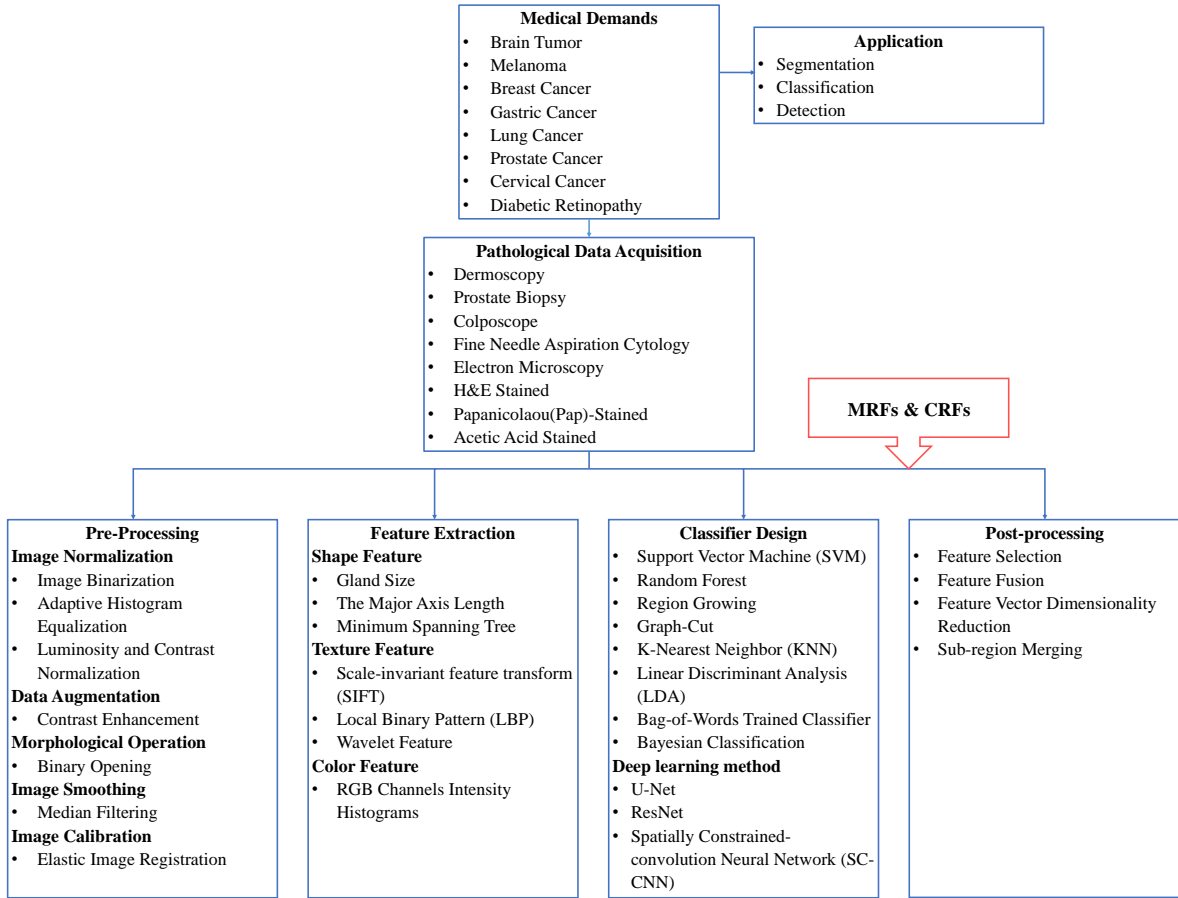


**Fig. 5** The conclusion of popular machine learning algorithm for pathology image analysis , consisting of image acquisition, image pre-processing, feature representation, classifier design and image post-processing.

**Table 1** Detailed information of frequently-used retinal datasets.

Datasets	Reference	Download Link	Quantity of dataset	Resolution (pixels)
DRIVE	[41]	<a href="http://www.isi.uu.nl/Research/Databases/DRIVE/">http://www.isi.uu.nl/Research/Databases/DRIVE/</a>	40	565 × 584
STARE	[42]	<a href="http://cecas.clemson.edu/~hoover/stare/">http://cecas.clemson.edu/~hoover/stare/</a>	81	700 × 605
CHASEDB1	[43]	<a href="https://blogs.kingston.ac.uk/retinal/chasedb1/">https://blogs.kingston.ac.uk/retinal/chasedb1/</a>	28	1280 × 960
HRF	[44]	<a href="https://www5.cs.fau.de/research/data/fundus-images/">https://www5.cs.fau.de/research/data/fundus-images/</a>	45	3304 × 2336
DRION	[45]	<a href="https://zenodo.org/record/1410497#.X1RFKMcgY2w">https://zenodo.org/record/1410497#.X1RFKMcgY2w</a>	110	923 × 596
MESSIDOR	[46]	<a href="http://www.adcis.net/en/third-party/messidor/">http://www.adcis.net/en/third-party/messidor/</a>	1200	1440 × 960, 2240 × 1488 or 2304 × 1536

### 2.1.3 Inference of MRFs

Given an observation of the feature vectors  $Y$ , the states  $X$  is to be estimated. The preferred method is an MAP estimation which entails maximizing the following quantity defined in Eq. 2 over all  $x \in \Omega$ :

$$\begin{aligned}
 P(x | y) &= \frac{P(y | x)P(x)}{P(y)} \\
 &\propto P(y | x)P(x)
 \end{aligned} \tag{2}$$

The first term of Eq. 2 indicates the impact of the feature vectors. Given their association  $X_s$ , to simplify

the problem, it is possible to assume that all  $Y_s$  are conditionally independent and that they have the same distribution. This means that if the class  $X_s$  of site  $s$  is known, then the classes and characteristics of the remaining sites do not offer additional information when evaluating  $Y_s$ , and the conditional distribution of  $Y_S$  is the same for all  $s \in S$ . Thus, Eq. 3 is derived and shown

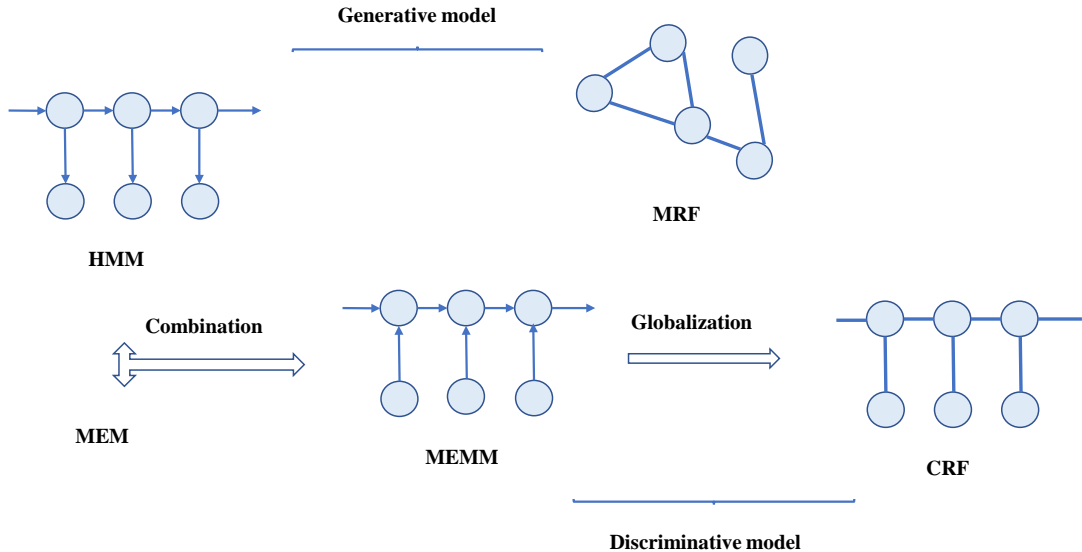


**Fig. 6** The emergence background of the MRF and CRF models (Maximum Entropy Model (MEM), Maximum Entropy Markov Models (MEMMs), Hidden Markov Model (HMM)).

**Table 2** The definition and brief introduction of the key mathematical symbol in random fields.

Mathematical symbol	Description
$S = \{1, 2, \dots, N\}$	The set containing $N$ sites to be classified
$s \in S$	The site belongs to set $S$
$X_s \in \Lambda \equiv \{\omega_1, \omega_2, \dots, \omega_L\}$	State (class) of each site
$Y_s \in \mathbb{R}^D$	$D$ -dimensional feature vector of each site
$x_s \in \Lambda$	Particular instances of $X_s$
$y_s \in \mathbb{R}^D$	Particular instances of $Y_s$
$\mathbf{X} = (X_1, X_2, \dots, X_N)$	All random variables $X_s$
$\mathbf{Y} = (Y_1, Y_2, \dots, Y_N)$	All random variables $Y_s$
$\Omega = \Lambda^N$	The state spaces of $\mathbf{X}$
$\mathbb{R}^{D \times N}$	The state spaces of $\mathbf{Y}$
$\mathbf{x} = (x_1, x_2, \dots, x_N) \in \Omega$	Instances of $\mathbf{X}$
$\mathbf{y} = (y_1, y_2, \dots, y_N) \in \mathbb{R}^{D \times N}$	Instances of $\mathbf{Y}$
$G = \{S, E\}$	An undirected graph structure on the sites, $S$ and $E$ are the vertices (sites) and edges
$\eta_s$	A neighborhood set contains all sites that share an edge with $s$
$P$	A probability measure defined over $\Omega$
$(G, \Omega, P)$	Random field

as follows:

$$\begin{aligned}
 P(y | x) &= \prod_{s \in S} P(y_s | x_s) \\
 &= \prod_{s \in S} p_f(y_s | x_s),
 \end{aligned} \tag{3}$$

The use of the single PDF  $p_f$  in Eq. (3) demonstrates that  $P(y_s | x_s)$  is uniformly distributed across  $S$ . The second term in Eq. 3 indicates the impact of the class labels. Generally, it is intractable to model this high-dimensional PDF. Nevertheless, its formulation will be obviously simplified if the Markov property is assumed.

Hammersley-Clifford (Gibbs-Markov equivalence) theorem shows the connection between the Markov property and the JPDF of  $\mathbf{X}$ , which indicates that a random field  $(G, \Omega, P)$  with  $P(\mathbf{x}) > 0$  for all  $\mathbf{x} \in \Omega$  satisfies the Markov property when it can be expressed as a Gibbs distribution in Eq. 4:

$$P(\mathbf{x}) = \frac{1}{Z} \prod_C V_C(\mathbf{x}), \tag{4}$$

where  $V_C(\mathbf{x})$  denotes the potential function on the clique  $C$ .  $Z = \sum_{\mathbf{x} \in \Omega} \prod_C V_C(\mathbf{x})$  is the normalization factor. A clique  $C$  is a subset of the vertices, and  $C \subseteq S$ , such that every two distinct nodes are adjacent in an undirected graph  $G = (S, E)$  [48].

## 2.2 Basic Knowledge of CRFs

Supposing  $\mathbf{Y}$  is a random variable of the data sequences to be labeled, and  $\mathbf{X}$  is a random variable representing the corresponding label sequences. If  $G = (S, E)$  is an undirected graph such that  $\mathbf{X} = (X_s)_{s \in S}$ , so that  $X$  is indexed by the vertices of  $G$ . Then assuming  $(\mathbf{X}, \mathbf{Y})$  is a CRF, when condition on  $\mathbf{Y}$ , the random variables  $\mathbf{X}_s$  obey the Markov property mentioned before. Compared

with the MRF model, a conditional model  $p(\mathbf{X} \mid \mathbf{Y})$  from paired observation and label sequences, and not explicitly model the marginal  $p(\mathbf{Y})$  [11]. The CRF can be represented by Eq. 5 as follows.

$$\begin{aligned} P(x \mid y) &= \frac{1}{Z(y)} \exp\left(\sum_{i,k} \lambda_k t_k(x_{i-1}, x_i, y, i)\right. \\ &\quad \left. + \sum_{i,j} \mu_j s_j(x_i, y, i)\right) \\ Z(y) &= \sum_x \exp\left(\sum_{i,k} \lambda_k t_k(x_{i-1}, x_i, y, i)\right. \\ &\quad \left. + \sum_{i,j} \mu_j s_j(x_i, y, i)\right) \end{aligned} \quad (5)$$

In this form,  $t_k$  and  $s_j$  are the feature function depending on the positions, where  $t_k$  is the transition feature function defined on the edge. It represents a feature in transmission from one node to the next and is dependent on the current positions.  $s_j$  denotes the state feature function that is dependent on the current location, representing the characteristics of the node.  $\lambda_k$  and  $\mu_j$  are learning parameters that are going to be estimated, and  $Z(y)$  denotes the normalization factor, which performs a sum over all possible output sequences [8].

### 2.3 Optimization Algorithm

In this subsection, some representative optimization algorithms frequently used in the related works are introduced. Most of them are iterative models applied for the observation estimation from known distributions.

#### 2.3.1 Expectation-maximization (EM)

Mixed models (such as random field models) can be fitted with maximum likelihood through the EM method without data. The algorithm first takes the initial model parameters as a priori and then uses them to estimate the missing data. Once achieving the complete data, the likelihood expectation maximization will be repeatedly performed to estimate the parameters of the model. The algorithm contains the expectation and maximization step. The optimal parameters estimation is inferred in each step, thereby achieving the best data [49].

#### 2.3.2 Iterative Conditional Modes (ICM)

ICM is an iterative and intuitive approach that utilizes knowledge of neighborhood system for optimal solution inference.  $P(X \mid Y)$  or a random selection serves as initial conditions of the method. If the new solution owns

the lowest energy, ICM attempts to use the current solution to upgrade the label at each position. When the energy at any position cannot be further reduced, the algorithm converges [50].

#### 2.3.3 Simulated Annealing

Simulated Annealing is a classical technique for optimization. It simulates the process of annealing to find global minimums or maximums from local minimum or maximums [50].

## 3 MRFs for Pathology Image Analysis

In this section, the related research papers focusing on pathology image analysis using the MRF methods are grouped into two basic categories and surveyed, including application in segmentation and other tasks. Finally, a conclusion of method analysis is presented in the last paragraph.

### 3.1 Image Segmentation Using MRFs

In the research of tuberculosis disease, the quantification of immune cell recruitment is necessary. Considering that fact, in [51], an automatic cell counting method for histological image analysis containing color image segmentation is introduced. In this research, a new clustering approach based on a simplified MRF model is developed, which is called the MRF clustering (MRFC) method. It uses the Potts model as a basic model, which is defined in eight connexity using second order cliques and is able to handle both color and spatial information. They also complement the MRFC with a watershed on the binary segmentation result of aggregated zones (whose size is higher than a threshold value). This method uses seven groups of mouse lung slice images for testing and gets a cell counting accuracy of 100% in a group containing 23 images.

An essential task for hematologists and pathologists is to isolate the nucleus and cytoplasmic areas in images of blood cells. This paper introduces a three-step image segmentation method in [52]. In the first step, an initial segmentation is completed using a Histogram Thresholding method. In the second step, a Deterministic Relaxation method, where the MRFs is utilized to formulate the MAP criterion, is adopted to smooth the noise area in the last step. Finally, a separation algorithm consisting of four steps is used: boundary smoothing, concavities detection, searching a pair of contour to be connected, and deleting the false subregion. The proposed segmentation algorithm is employed to 22 cell

images, containing four different kinds, and it yields 100% correct results (the illustration of the experimental results is presented in Fig. 7).

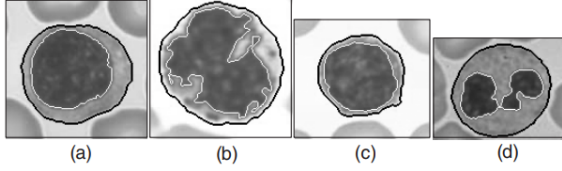


**Fig. 7** Segmentation results without tangent red blood cell. This figure corresponds to Fig.4 in [52].

In [53], a couple method of the MRF and fuzzy clustering is adopted to express the adapt function and segment pathological images. In addition, particle swarm optimization (PSO) is added to the fuzzy clustering method. Thus, this model has the strong capability of noise immunity, quick convergence rate and powerful ability of global search. On a 821-cell dataset, an accuracy value of 86.45% is finally achieved.

In order to detect and grade the degree of lymphocyte infiltration (LI) in HER2+ breast cancer histopathology images automatically, a quantitative CAD system is developed in [54]. The lymphocytes are located with the integration of region growing and the MRF method first (the flow chart is shown in Fig. 8). The Voronoi diagram, Delaunay triangulation diagram, and minimum spanning tree diagram are applied. The center of lymphocytes detected separately serve as the vertex. After feature extraction from each sample, the non-linear dimensionality reduction scheme is applied to produce dimensionality reduction embedded space feature vector. Finally, an SVM classifier is adopted to distinguish the samples with high or low LI in the dimensionality reduction embedded space. In the first step, after Bayesian Modelling of LI via MAP estimation, an MRF model defines the prior distribution  $p(x)$ , using ICM as an optimization algorithm to assign a hard label to each random variable. Afterward, each region is classified as either breast cancer or lymphocyte nucleus. In this experiment, totally 41 H&E stained breast biopsy samples are tested, yielding an accuracy value of 0.9041.

In [55], a four-step image segmentation process is employed to classify four categories of teratoma tissues. First, the image segmentation process is formulated in the Bayesian framework. Second, a set of hidden real-valued random fields designing a given segmentation probability is introduced. In order to produce smooth fields, a Gaussian MRF (GMRF) prior is assigned to reformulate the original segmentation problem. This method's salient feature is that the original

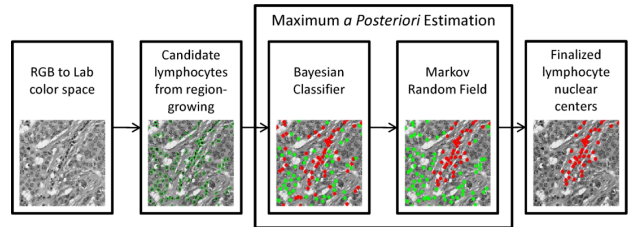


**Fig. 8** The flowchart explains the main five steps in the automated lymphocyte detection framework. This figure corresponds to Fig.3 in [54].

discrete optimization is transformed into a convex optimization problem, which makes it easier to use related tools to solve the problem accurately. Third, the form of total variation of isotropic vectors is adopted. Finally, aiming to conquer the convex optimization problem that makes up the MAP inference of hidden field, the Segmentation via a Constrained Split Augmented Lagrangian Shrinkage Algorithm (SegSALSA) segmentation is introduced. As Fig. 9 shown, the proposed system with SegSALSA finally yields an accuracy value of 0.84.

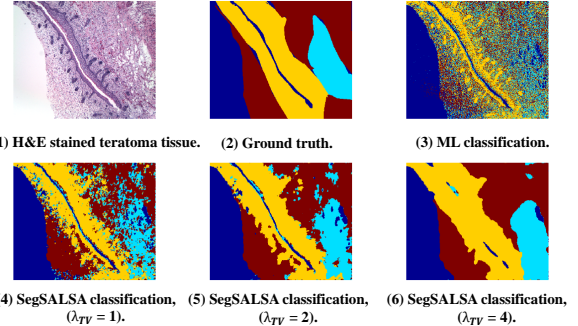


**Fig. 9** H&E stained teratoma tissue sample consisting four classes of cell, which is imaged under 40X magnification microscope. The detailed information of this figure can be seen in Fig.4 in [55].

The morphology of retinal vessels and optic disc is an important consideration to the diagnosis of many retinal diseases, such as diabetic retinopathy (DR), hypertension, glaucoma. Given that fact, in [56], an MRF image reconstruction method is applied to segment the optic disk. The first step is to extract the retina vascular tree applying the graph cut technique so that the location of the optic disk can be estimated on the basis of the blood vessel. Afterward, the MRF method is adopted to define the location of the optic disk. It plays a significant role in eliminating the vessel from the optic disk area and meanwhile avoids other structural modifications of the image. Fig. 10 (a) and (b) illustrate the

optic disk segmentation results, compared with other prevalent methods. On the DRIVE dataset, an average overlapping ratio 0.8240, mean absolute distance 3.39, and sensitivity 0.9819 are finally achieved.

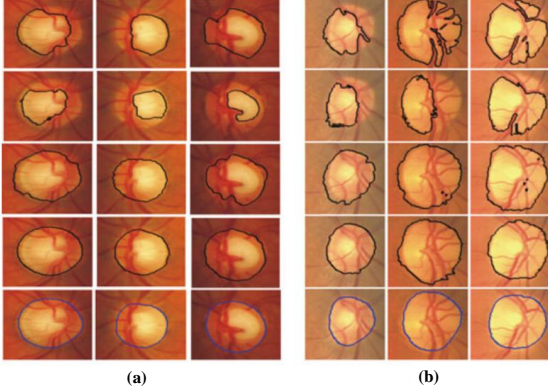


**Fig. 10** The illustration of optic disk segmentation results tested on DIARETDB1 and DRIVE dataset. This figure corresponds to Fig.14 in [56].

In [57], aiming to improve Melanoma's early diagnosis accuracy, an overall process research based on dermoscopy images is proposed, including image noise removal, lesion region segmentation, feature extraction, recognition of skin lesions and its classification. Lesion region segmentation is the first and essential step, where the image noise is removed first using contrast enhancement method, threshold and morphological method. In the main part, a fusion segmentation algorithm applying the MRF segmentation framework is introduced to develop the robustness of a single segmentation algorithm. The fusion strategy transforms the optimal fusion segmentation problem into the problem of minimizing the multi-dimensional space energy composed by the results of four segmentation algorithms (Statistical Region Merging, Adaptive Thresholding, Gradient Vector Flow Snake and Level Set). 1039 RGB images derived from two European universities are used for training and the overall process research finally achieves classification accuracy 94.49%, sensitivity 95.67% and specificity 94.31%.

Nuclei segmentation is one of the essential steps for breast histopathology image analysis. To detect the nuclei boundary, a four-stage procedure is proposed in [58]. In the preprocessing step, the enhanced grayscale images are obtained by using the principal component analysis (PCA) method. Second, the nuclei saliency map is constructed applying tensor voting. Thirdly, loopy belief propagation on the MRF model is applied to extract the nuclei boundary. At this stage, researchers determine the nuclear boundary by a set of radial profiles

with equal arc-length intervals from the window edge to the window center, which is illustrated in Fig. 11(a)). The MRF observable node variable is the intensity value in the polar form of the nuclear significance graph. Meanwhile, the hidden node variable is the radial profile of the nuclear boundary points, which is shown in Fig. 11(b). Finally, spurious nuclei are detected and removed after threshold processing. In a breast histopathology image containing 512 nuclei, the proposed system gets a nucleus segmentation precision of 0.9657, recall of 0.7480, and Dice coefficient of 0.8830, respectively.

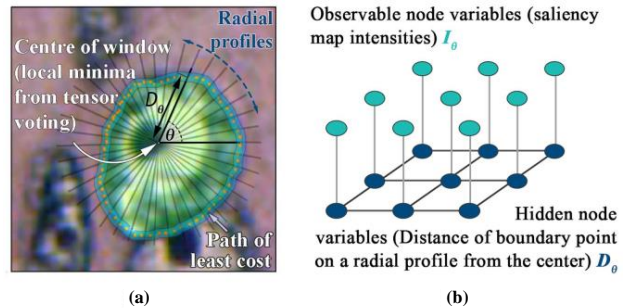


**Fig. 11** a) Graphical illustration of the essential step in boundary delineation problem. b) Probabilistic graphical model of the MRF applied in this paper. The detailed information of this figure can be seen in Fig.5 in [58].

In [59], an MRF-based novel microaneurysms (MA) segmentation method is developed for DR detection in the retina, where the vessel network is first removed using a contrast enhancement method, then the MA candidates are extracted using local applying of the MRF. Lastly, an SVM classifier is designed to identify true MAs employing 23 features. Based on the motivation of our review, we only concentrate on the MA candidate extraction technique. The EM algorithm is applied for the mean and variance estimation of each category. Moreover, the main equation optimization is conducted with a simulated annealing algorithm. But the MRFs have two limitations: Firstly, the number of regions to be selected after segmentation by the MRFs is so large that the false positive rate may increase; second, the size of some MAs might change, so they cannot represent true MAs anymore. To overcome these limitations, the region growing algorithm is used, where some regions are finally marked as non-MAs and precluded from becoming candidate regions. The authors manage to achieve an average sensitivity value of 0.82 on the publicly available dataset DIAREDB1.

In [60], a novel superpixel-based MRF framework is proposed for color cervical smear image segmentation, where the SLIC algorithm generates the superpixels and a feature containing a 13-dimensional vec-

tor is extracted from each superpixel first. Second, initial segmentation results are provided by  $k$ -means++. Finally, images are modeled as an MRF, making the edges smoother and more coherent to semantic objects. An iterative adaptive classified algorithm is adopted for parameter estimation. Moreover, This study introduces a gap search algorithm to speed up iteration, which only updates the energy of critical local areas, such as edge gaps. The best results are achieved on Herlev public dataset, yielding 0.93 Zijdenbos similarity index (ZSI) [61] of the nuclei segmentation.

In [50], an MRF-ANN algorithm is developed for estrogen receptor scoring using breast cancer immunohistochemical images, where the white balancing method is first applied for color normalization, then the MRF model with EM optimization is adopted to segment the ER cells. In addition,  $k$ -means clustering is utilized to obtain the initial labels of the MRF model. Lastly, based on the pixel color intensity feature, an artificial neural network (ANN) is employed to obtain an intensity-based score of ER cells. Using the standard Allred scoring system, the final ER score is calculated by adding intensity and proportion scores (calculating the percentage of ER-positive cells from the cell count). On a dataset from a medical center in India, the proposed segmentation method finally achieves an F-measure of 0.95 in tissue sections of 65 patients.

In [62], a CAD framework is introduced for cancerous cell nuclei analysis. The images are obtained from pap-stained microscopic images of lung Fine Needle Aspiration Cytology (FNAC) sample, which is essential for lung cancer diagnosis. First, edge-preserving bilateral filtering is used for noise removal. Afterward, the Gaussian mixture model-based hidden Markov random field model is applied to segment the nucleus. Then, the bag-of-visual words model is applied to classify the kernel. The scale-invariant feature transformation features are extracted from the candidate kernel, and the random forest classifier model is trained with these features. A hidden Markov random field, as well as its Expectation-Maximization, is employed in the segmentation step to finding out the unknown parameters in the potential function. This algorithm needs morphological post-processing, including morphological opening operation, watershed algorithm, and connected components labeling method. The segmentation process yields a specificity and sensitivity value of 97.93% and 98.88%.

A two-level segmentation algorithm based on spatial clustering and the HMRFs is proposed in [63] to improve the segmentation accuracy of cell aggregation and adhesion region. First,  $k$ -means++ clustering is employed to obtain the initial labels of MRFs based on the color feature of pixels in the Lab color space.

Second, the spatial expression model of the cell image is constructed by the HMRF, which considers the spatial constraint relation in order to limit the influence of isolated points and smooth segmentation areas at the same time. Finally, the EM algorithm is adopted for model parameter optimization. Meanwhile, the results are finally refined by the iterative algorithm. The experiment is based on the 61 bone marrow cell images from Moffitt Cancer Center, and after ten iterations, the proposed method yields an accuracy value of 0.9685.

### 3.2 Other Applications Using MRFs

#### 3.2.1 Prostate Cancer Detection from a US Research Team

A joint research group from the USA, leading by researchers from Rutgers University and the University of Pennsylvania, develops a serial work about Computer-Aided Detection of Prostate Cancer (CaP) on Whole-Mount Histology. These researches share almost the same procedure, and the MRFs are mostly used in the classification part, which shows exciting performance improvement.

In [64], a CAD algorithm is developed to detect the CaP in low resolution whole-mount histological sections (WMHSs). In addition to the area of the glands, another distinguishing feature of glandular cancers is that they are close to other cancerous glands. Therefore, the information in these glands is modeled using the MRF model. The process of the CAD algorithm can be concluded into three steps: First, the region growing algorithm is applied to gland segmentation in the luminance channel of H&E stained samples. Second, the system calculates the morphological characteristics of each gland and then classifies them through Bayesian classification to mark the glands as malignant or benign. Third, the labels obtained in the last process are applied in MRF iteration to generate the final label. In this step, unlike most of the MRF strategies (such as the Potts model), which rely on heuristic formulations, a novel methodology allowing the MRFs to be modeled directly from training data is introduced. The proposed system is tested in four H&E stained prostate WMHSs, achieving a sensitivity and specificity value of 0.8670 and 0.9524, respectively, for cancerous area detection.

As an extension of this work, in [65], aiming to solve the disadvantages of the traditional random fields that most of them produce a single, hard classification at a static operating point, the weighted maximum a posteriori (WMAP) estimation and weighted iterated conditional modes (WICM) are introduced. The use of these

two algorithms proves to have good performance in 20 WMHSs from 19 patients' images.

Based on the work above, in [47] and [66], the probabilistic pairwise Markov models (PPMMs) are presented. Compared to the typical MRF models, PPMMs, using probability distributions instead of potential functions, have both more intuitive and expansive modeling capabilities. In Fig. 12, an example of the WMHS image detection steps is shown. In the experiment in [47], 20 prostate samples obtained from 19 patients in two universities are used for testing. When specificity is held fixed at 0.82, the sensitivity and area of the ROC curve (AUC) of the PPMMs increase to 0.77 and 0.87, respectively (compared to 0.71 and 0.83 using Potts model).

In [66], as a supplement to the previous research, the research team hopes to develop a comprehensive and hierarchical algorithm that can finish cancerous areas detection at high speed under a lower resolution, and then refine the results at a higher resolution, and finally perform Gleason classification. The researchers use this method to detect 40 H& E stained tissue sections of 20 patients undergoing radical prostatectomy in the same hospital, and find that the sensitivity and specificity of CaP detection are 0.87 and 0.90, respectively.

It is found that most of the published researches limit the MRF performance to a single, static operating point. To solve this limitation, in [67], weighted maximum posterior marginals (WMMPM) estimation is developed, whose cost function allows the penalty for being classified incorrectly with certain classes to be greater than for other classes. The realization of WMMPM estimation needs to calculate the posterior marginal distribution, and the most popular solution is the Markov Chain Monte Carlo (MCMC) algorithm. As an extension of the MCMC method, EMCMC has the same simple structure but better results. It is applied for accurate posterior marginals estimation. This data set includes 27 digitized H&E stained tissue samples from 10 patients with RPs. By quantitatively comparing the ROC curves of the E-MCMC method and other MCMC methods, experiments prove that this method has better performance.

Based on the work above, a system for detecting regions of CaP using the color fractal dimension (CFD) is established in [68]. In order to find the most suitable hyper-rectangular boundary size for each channel, the researchers improve the traditional CFD algorithm and analyze the values of the three channels in the image separately. And then, the authors combine the probability map constructed via CFD with the PPMM introduced in the above research. In the experiment, an AUC of 0.831 is achieved on a dataset from 10 patients, containing 27 H&E stained histological sections.

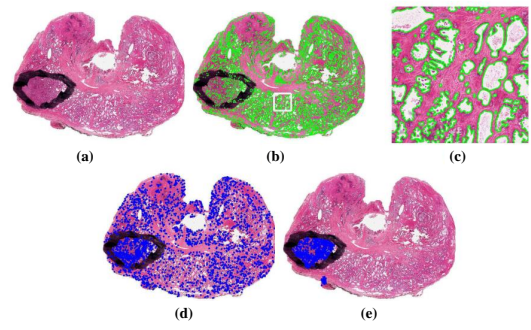


**Fig. 12** The illustration of ground truth and segmentation performance of the mentioned methods. The detailed information of this figure can be seen in Fig.3 in [47].

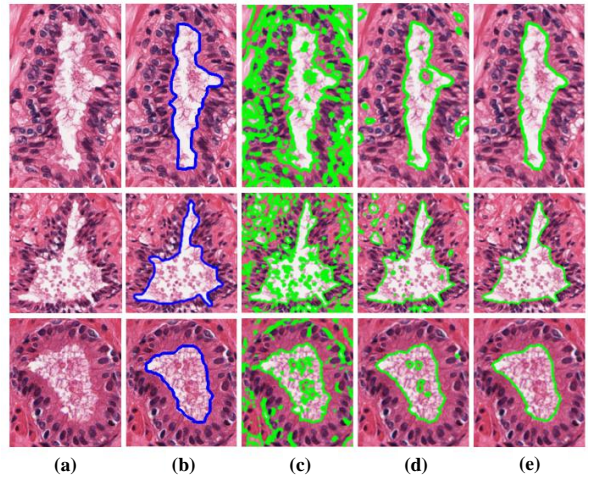


**Fig. 13** Method comparison using some segmentation results example for prostate cancer analysis in biopsy. This figure corresponds to Fig.2 in [69].

The research team also proposes literature focusing on automated segmentation methods. In [69], an MRF driven region-based active contour model (MaRACel) is presented for segmentation tasks. One limitation of most RAC models is the assumption that images of each spatial location is statistically independent. Considering that fact, the MRF prior is combined with the AC model to consider the relationship between different spatial location information. The results tested on 200 images from prostate biopsy samples show that the average sensitivity, specificity and positive predictive value were 71%, 95%, and 74%, respectively. Fig. 13 shows segmentation results comparison between the proposed method and other methods.

In [70], the preliminary work is extended. The authors introduce a method for incorporating an MRF energy function into an AC energy functional –an energy functional is the continuous equivalent of a discrete energy function. The MaRACel is also tested in the task of differentiation of Gleason patterns 3 and 4 glands (the

flowchart is shown in Fig. 14), beside the segmentation of glands task. The proposed methodology finally gets gland segmentation Dice of 86.25% in 216 images and Gleason grading AUC of 0.80 in 55 images obtained from 11 patient studies from the Institute of Pathology at Case Western Reserve University.

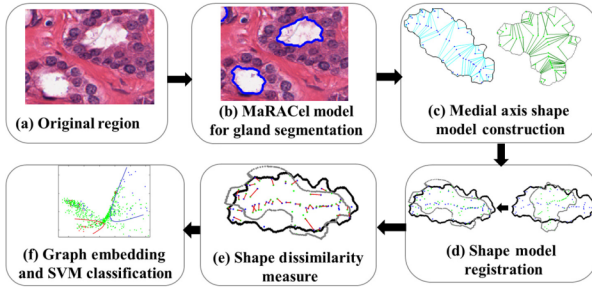


**Fig. 14** The work-flow of MaRACel model for gland segmentation as well as explicit shape descriptors for Gleason grading. This figure corresponds to Fig.1 in [70].

### 3.2.2 Works of Other Research Teams

For the purpose of assisting pathologists in classifying meningioma tumors correctly, a series of texture features extraction and texture measure combination methods are introduced in [71]. A Gaussian Markov random field model (GMRF) is employed, which contains three order Markov neighbors. Seven GMRF parameters are inferred applying the least square error estimation algorithm. The combined GMRF and run-length matrix texture measures on a set of 80 pictures are proved to outperform all other combinations (e.g. Co-occurrence matrices, fractal dimension et al.) considering the performance of quantitatively characterizing the meningioma tissue, obtaining an overall classification accuracy of 92.50%.

In [72–74], a hierarchical conditional random field (HCRF) model is developed to localize abnormal (cancer) areas in gastric histopathology image. The post-processing step is based on the MRF and morphological operations for boundary smoothing as well as noise removal. The detail information of HCRF will be discussed in next section.

### 3.3 Summary

A summary of the MRF methods for pathology image analysis is illustrated in Table 3, which contains some essential attributes of the summarized research papers. Each row indicates publication year, reference,

research team, input data, disease, data preprocessing, segmentation and classification techniques, and the result of an individual paper. It can be concluded from the table that MRFs has a wide range of application in various disease detection, and mostly used in the diagnosis of CaP and eye disease. Histopathology images are the most common input data, cytopathology images followed. Among these researches, the MRF models are applied in segmentation and classification tasks in most cases, and they are also used for postprocessing in [72] and feature extraction in [71]. Besides, with MRF theory development, some researchers propose the model's improvement or variants, such as PPMM, GMRF, and Connecting MRF, whose modelling abilities are more expansive comparing to the classical the MRFs. Moreover, the feature extracted algorithm for classification is more complex over 20 years. Since 2015, advanced machine learning models (SVM, ANN, Random Forest et al.) have been integrated into related research serving as classifiers, and the final results are significantly improved in larger datasets compared to those who use Bayesian classifier.

## 4 CRFs for Pathology Image Analysis

In this section, unlike the MRFs concluded before, it is known that the CRFs take segmentation and classification tasks simultaneously. Instead, these researches are categorized into microscopic images and micro-alike (close-up/macro images) two images of analysis work by the input dataset's property.

Their main differences can be concluded into two points: magnification and application scenarios. Most of the work to obtain micro-alike image can be accomplished within the magnification range of  $2\times$  to  $15\times$ , such as endoscopy and ophthalmoscopy. On the contrary,  $20\times$  and  $40\times$  optical magnifications are most frequently used for acquiring microscopic images, such as examining tissues and/or cells under a microscope for cancer diagnosis. Due to their different property, they are used in different application scenarios. Take a colposcope as an example. A lower magnification yields a broader horizon as well as greater depth of field for the cervix examination. More magnification is not necessarily better, since there are certain trade-offs as magnification increases: the field of view becomes smaller, the depth of focus diminishes, and the illumination requirement increases [76]. When examining cells and tissues removed from suspicious 'lumps and bumps', and identifying whether they are from tumor or normal tissue, a microscope of high magnification is indispensable.

**Table 3** Summary of concluded papers for pathology image analysis using MRFs. ( Specificity (Sp), Positive predictive (PP), Overlapping ratio (Oratio), Sensitivity (Sn), Area of the ROC curve (AUC), Precision (P), Mean absolute distance (MAD), Dice (D), Recall (R), Zijdenbos similarity index (ZSI), Accuracy (Acc), Dice Coefficient (DC), F-measure (F), Prostate Cancer (CaP)).

Year, Ref, Research team	Disease	Input data	Task	Random field type	Optimization techniques	Feature extraction	Classification Result evaluation
2002, [51], Meas-Yedid et al.	–	Mouse lung slice, 23 images	Segmentation (cell nuclei, immune cells and background), Immune cell counting	MRF	–	–	Acc=100%.
2004, [52], Won et al.	–	Blood cell, 22 images	Segmentation (nucleus, cytoplasm, red blood cell , and background)	MRF	Deterministic relaxation	Smoothness constraint and high gray level variance	Acc=100%.
2008, [64], Monaco et al.	CaP	4 WMHSs	Identification and segmentation of regions of CaP	MRF	ICM	Square root of gland area	Bayesian classification Sn=86.7%, Sp=95.24%.
2009, [65], Monaco et al.	CaP	20 WMHSs	Identification and segmentation of regions of CaP	PPMM	WICM	Square root of gland area	Bayesian classification
2009, [47], Monaco et al.	CaP	20 WMHSs	Identification and segmentation of regions of CaP	PPMM	WICM	Square root of gland area	Bayesian classification Sn=77%, Sp=82%, AUC=0.87.
2009, [53], Zou et al.	–	821 cells	Segmentation	MRF	FCM with PSO	–	Acc=86.45%.
2009, [54], Basavan-hally et al.	Breast cancer	HER2+ H&E lymphocytes, 41 images	Identification and segmentation of regions of CaP	MRF	ICM	Voronoi diagram, Delaunay triangulation, and minimum spanning tree	Bayesian classifier, SVM Acc=90.41%.
2010, [66], Monaco et al.	CaP	40 WMHSs	Identification and segmentation of regions of CaP	PPMM	WICM	Square root of gland area	Bayesian classification Sn=87%, Sp=90%.
2010, [71], Al-Kadi et al.	Meningioma	Meningioma tumour, 80 images	Classification (malignant or benign)	GMRF	Least square error estimation	Fractal dimension, grey level co-occurrence matrix, grey level run-length matrix, GMRF	Bayesian classification Acc=92.50%.
2010, [69], Xu et al.	CaP	200 prostate biopsy needle images	Segmentation of prostatic acini	MRF	–	–	Sn=71%, Sp=95%, PP=74%.
2011, [68], Yu et al.	CaP	27 WMHSs	Identification and segmentation of regions of CaP	PPMM	ICM	CFD	Bayesian Classification AUC=0.831.
2011, [67], Monaco et al.	CaP	27 WMHSs	Identification and segmentation of regions of CaP	MRF	E-MCMC, M-MCMC	Gland area	WMPM classification
2014, [55], Bioucas-Dias et al.	Teratoma	Teratoma tissue, a 1600 × 1200 image	Classification of four categories of teratoma tissues	HMRF	EM based algorithm	–	– Acc=84%.
2014, [56], Salazar-Gonzalez et al.	Eye disease	Fundus retinal images, DI-ARETDB1, DRIVE, STARE public dataset	Segmenting of blood vessel and optic disk	MRF	Max-flow algorithm	–	Oratio=0.8240, MAD=3.39, Sn=98.19% (in DRIVE).

Year, Ref, Research team	Disease	Input data	Task	Random field type	Optimization techniques	Feature extraction	Classification	Result evaluation
2015, [57], Liu et al.	Melanoma	Melanoma in Demoscopy, 1039 images	Lesion region segmentation and classification (malignant or benign)	MRF	–	Symmetry, size, shape, maximum diameter, Gray level co-occurrence matrix, color features, SIFT	SVM classifier	Acc=94.49%, Sn=95.67%, Sp=94.31%.
2016, [58], Paramanandam et al.	Breast cancer	High-grade breast cancer images, 512 nuclei	Segmentation of the individual nuclei	MRF	Loopy Back Propagation	Tensor voting method	–	P=96.57%, R=74.80%, DC=88.3%.
2016, [59], Razieh et al.	Microaneurysms	Fundus retinal images, DIARETDB1 public dataset	Microaneurysms segmentation	MRF	Simulated annealing	Shape-based features, Intensity and color based features, Features based on Gaussian distribution of MAs intensity	SVM classifier	Sn=82%.
2016, [60], Zhao et al.	Cervical cancer	Color cervical smear images, Herlev and real-world datasets	Segmentation of cytoplasm and nuclei	MRF	Iterative adaptive classified algorithm	Pixel intensities and the shape of superpixel patches	–	Herlev: ZSI=0.93, 0.82; real-world: ZSI=0.72, 0.71 (cytoplasm, nuclei).
2017, [50], Mungle et al.	Breast cancer	Breast cancer immunohistochemical images, 65 patients' tissue slides	ER scoring	MRF	EM, ICM and Gibbs sampler (with simulated annealing)	R, G and B values of individual cell blobs	ANN	F=96.26%.
2017, [70], Xu et al.	CaP	600 prostate biopsy needle images	Segmentation of prostatic acini and Gleason grading	Connecting MRFs	[75]	SVM classifier	Segmentation: D=86.25%, Gleason grading: AUC=0.80.	
2018, [62], Dholey et al.	Lung Cancer	Papanicolaou-stained cell cytology, 600 image	Segmentation of the nucleus and classification (Small Cell Lung Cancer and Non-small Cell Lung Cancer)	GMM-HMRF	HMRF-EM	SIFT, K-Means Clustering, Construction of Visual Dictionary	Random Forest Training (Bag-of-Words)	Sn=98.88%, Sp=97.93%.
2019, [63], Su et al.	–	Bone marrow smear, 61 images	Segmentation	HMRF	EM	Color intensity	<i>k</i> -means	Acc=96.85%.

The related research papers are concluded first. Finally, a summary of method analysis is given in the last paragraph.

#### 4.1 Microscopic Image Analysis

In [77], a method based on multi-spectral data is proposed for cell segmentation. A CRF model incorporating spectral data during inference is developed. The loopy belief propagation algorithm is applied to calcu-

late the marginal distribution, which also solves the optimal label configuration problem. The proposed CRF model achieves better results because the spectral information describing the relationship between neighboring bands helps to integrate spatial and spectral constraints within the segmentation process. 12 FNA samples are used for testing, and the result shows that the CRF model could help to get over segmentation difficulties when the contrast-to-noise ratio is poor.

In [78], a method is proposed for identifying disease states by classifying cells into different categories. Single cell classification can be divided into three steps: Firstly, level sets and marker-controlled watershed algorithm are applied for cell segmentation. Second, wavelet packets is employed to extract the the cell feature. Finally, SVM and CRF are served as the classifiers. Image information is represented by CRF to characterize the features and distribution of adjacent cells, which plays an significant role in tissue cells classification task. Its potential is related to the output discriminant value of SVM. After initialization of the CRF, considering that most of cells do not regularly distribute over the tissue, an algorithm for determining the optimal graph structure on the basis of local connectivity is proposed. This method is tested in lung tissue images containing 9551 cells, yielding specificity 96.52%, sensitivity 48.30%, and accuracy 90.26%.

In [79], a novel method is presented for glandular structures detection using microscopic images of human colon tissues, where the images are transformed to polar space first, then a CRF model (shown in Fig. 15) is introduced to find the gland's boundary of and a support vector regression (SVR) based on visual characteristics is proposed to evaluate whether the inferred contour corresponds to a real gland. In the final step, the results of the previous step combined with these two methods are utilized to find the GlandVision algorithm ranking of all candidate contours, and then generate the final result. In the inference process of the CRF, two chain structures are applied to approximate this circulate graph, which uses Viterbi algorithm to find the optimal results. The authors use the combination of cumulative edge map and the original polar image to generate the unary potential and the Gaussian edge potential as the pairwise potential. Besides, the thresholding algorithm is applied to eliminate most of the false positives regions generated in this step. Finally, a segmentation accuracy of 0.732 is achieved on the dataset containing 20 microscopic images of human colon tissues for training and testing (shown in Fig. 16). Based on the work above, in [80], a task called inter-image learning is introduced, which predicts whether those sub-images containing glands. A linear SVM is applied to tackle this problem, using the sum of the node potential of the CRF in contour detection task along with other mid-level features (listed in Table 4 in detail). This research also finds that all the gland contours proposed by the random field which rank according to the learned SVM score achieves the best result compared to other index, so it is used as the final output of the CRF. Based on the same dataset, this method gets an accuracy of 80.4%. Beside the grey-scale images, it is

also tested in 24 H&E stained images, yielding sensitivity 82.35%, specificity 93.08%, accuracy 87.02% and Dice 87.53%.

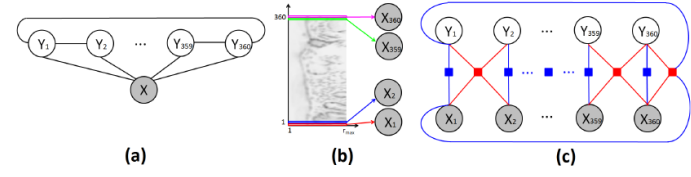


**Fig. 15** A circular area with radius of  $r_{max}$  is converted to a fixed size polar image of 360 rows  $\times r_{max}$  columns after the transformation mentioned in the article. This figure corresponds to Fig.2 in [79].

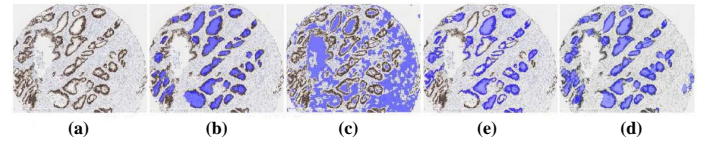


**Fig. 16** Segmentation results of different approaches. The detailed information of this figure can be seen in Fig.20 in [79].

A system is presented to segment necrotic regions from normal regions in brain pathology images based on a sliding window classification method followed by a CRF smoothing in [29]. First, four features are extracted and encoded by Bag-of-words (BoW) algorithm. Then, an SVM classifier is applied in the sliding windows using the features extracted in the last step. Thirdly, the CRF model is applied to discard noisy isolated predictions and obtain the final segmentation with smooth boundaries. The node and edge potentials of the CRF is defined using the probability map provided by SVM. In 35 training data provided by the MICCAI 2014 digital pathology challenge, the proposed method gets a segmentation accuracy value of 0.66.

In [81], an end-to-end algorithm is proposed based on fully convolutional networks (FCN) for inflammatory bowel disease diagnosis to recognize muscle and messy areas. For purpose of incorporating multi-scale information into the model, a specific field of view (FOV) method is applied. The structure of multi-scale FCN is as follows: First, different FCNs are used to make each FCNs process the input image with a different FOV; then, the results of these FCNs are merged to form a score map; finally, the fusion score map is computed through the soft-max function for the cross-entropy classification loss calculation. The CRFs are severed as post-processing method of FCN. It takes the probability generated by the FCN as the unary cost, and also con-

siders the pairwise costs, so that the results are smooth and consistent. Tested in 200 whole slides images of H&E stained histopathology tissue, the authors manage to achieve an accuracy of 90%, region intersection over union (IU) of 56%.

The degree of deterioration of breast cancer is highly related to the number of mitoses in a given area of the pathological image. Considering that fact, a multi-level feature hybrid FCNN connecting a CRF mitosis detection model is proposed in [82]. On the open source ICPR MITOSIS 2014 dataset, the proposed classification methodology is found to have F-score 0.437.

In [83], a cell image sequence morphology classification method based on linear-chain condition random field (LCRF) is presented. Firstly, this problem is modelled as a multi-class classifier based on LCRF, a conditional probability distribution model assuming that  $X$  and  $Y$  own identical structure. Then, a series of features are extracted to describe the internal motion for cells image sequence, including deformation factor and dynamic texture. Lastly, the model parameter is estimated by discrimination learning algorithm called margin maximization estimation and the image sequence classification result is produced according to the input feature vectors. The effectiveness of the model is verified on micro image sequence data set of pluripotent stem cells from University of California, Riverside, USA, yielding an accuracy value of 0.9346.

In [84], a neural conditional random field (NCRF) DL framework is proposed to detect cancer metastasis in WSIs. The NCRF is directly incorporated on top of a CNN feature extractor (called ResNet) forming the whole end-to-end algorithm. Fig. 17 illustrates the overall architecture of the NCRF. Specifically, the authors use the mean-field inference to approximate marginal distribution of each patch label. Then, after the network calculates the cross-entropy loss, the entire model is trained using the back propagation algorithm. On the Camelyon16 dataset, including 270 WSIs for training, 130 tumor WSIs for testing, an average free response receiver operating characteristic (FROC) score of 0.8096 is achieved finally.

To recognize cancer regions of pathological slices of gastric cancer, a reiterative learning framework is proposed in [85], which first extracts the region of interest in diagnosis process, then the patch-based FCN is trained, and finally uses the FC-CRF to perform overlap region prediction and post-processing operations. However, the performance of the CRF in their task is not satisfactory, because several erroneous data distributions in such weak annotation task may lead to bad performance. After adding the CRF to the model, a mean intersection over union Coefficient (IoU) value in

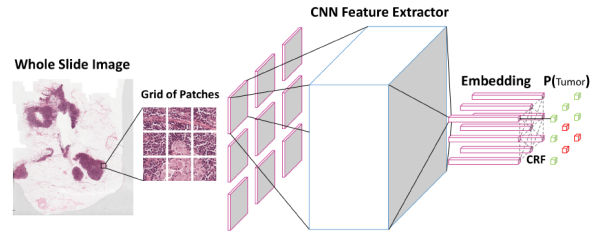


**Fig. 17** The architecture of NCRF model. This figure corresponds to Fig.1 in [84].

test set decreases from 85.51% to 84.85%. Based on the work above, this research team improves the network structure, proposing a deeper segmentation algorithm deeper U-Net (DU-Net) in [86]. In this case, post-processed with the CRF is proved to boost the performance and the IoU value increases to 88.4% in the same dataset.

A method using weak annotations for nuclei segmentation is proposed in [87]. Firstly, in order to derive complementary information, the Voronoi label and cluster label which serve as the initial label are generated with the points annotation image. Second, label produced in last step is employed to train a CNN model. Dense CRFs are embedded into the loss function to further refine the model. In the experiment, lung cancer and MultiOrgan dataset are used for testing, both achieving accuracy over 98%. The result is shown in Fig. 18.

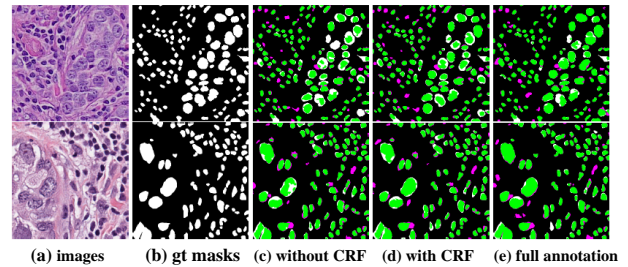


**Fig. 18** Comparison of weakly and fully supervised training. This figure corresponds to Fig.4 in [87].

A cell segmentation method with texture feature and spatial information is developed in [88]. In the first step, features are extracted and utilized to train machine learning model, providing pre-segmentation result. In the second step, the image is post-processed by MRF and CRF model for binary denoising. The proposed segmentation methodology obtains F-score, Kappa and overall accuracy of 86.07%, 80.28% and 91.79%, respectively.

Inspired by the way pathologists perceive the regional structure of tissue, a new multi-resolution hierarchical network called SuperCRF is introduced in [89] to improve cell classification. A CNN that considers spatial constraint is trained for WSIs detection and classification. Fig. 19(a) illustrates this network clearly. Then, a CRF, whose architecture is shown in Fig. 19(b), is trained by combining the adjacent cell with tumor region classification results based on the super-pixel machine learning network. Subsequently, the labels of the CRF nodes representing single-cell are connected to the regional classification results from superpixels producing the final result. Segmentation accuracy, precision and recall of 96.48%, 96.44%, and 96.29% are achieved on 105 images of melanoma skin cancer, shown in Fig. 19(c).

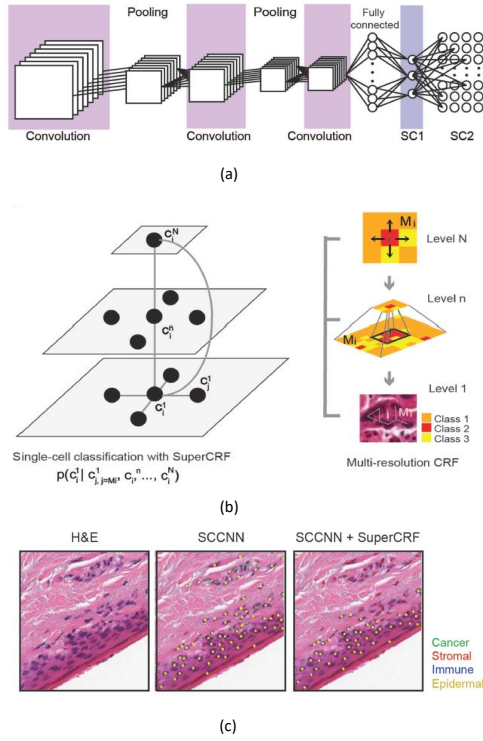


**Fig. 19** Overview of the SuperCRF framework for melanoma image analysis. This figure corresponds to Fig.1 in [89].

In [72–74], a gastric histopathology image segmentation method based on HCRF is introduced for abnormal regions detection. The structure of the HCRF model is presented in Fig. 20(a). Firstly, a DL network U-Net is retrained to construct pixel-level potentials. Meanwhile, for purpose of building up patch-level potentials, the authors fine tune another three CNNs, including ResNet-50, VGG-16, and Inception-V3. Adding pixel-level and patch-level potentials contribute to in-

tegrate information in different scales. Besides, binary potentials of their surrounding image patches are formulated according to the ‘lattice’ structure described in Fig. 20(b)(c). When the HCRF model is constructed, the post-processing operation is finally adopted to refine the results. Researchers test the performance of HCRF on a public gastric histopathological image dataset containing 560 images, achieving 78.91% segmentation accuracy.

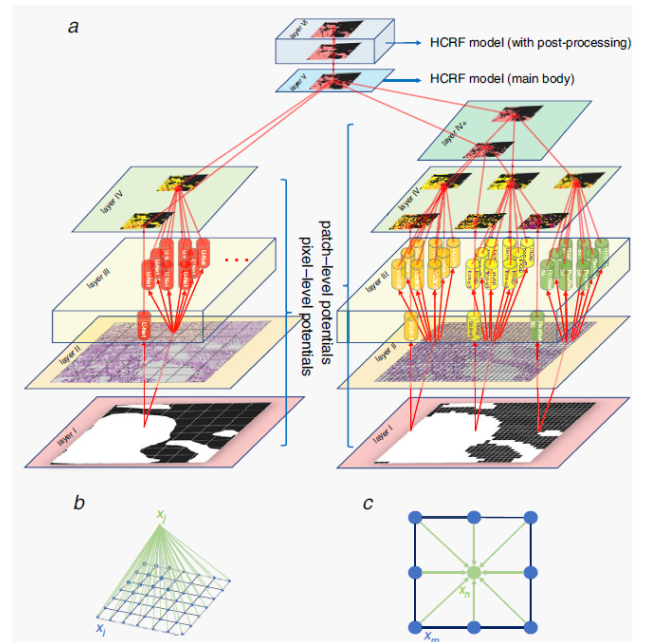


**Fig. 20** Overview of HCRF framework for gastric histopathological image analysis. This figure corresponds to Fig.2 in [72].

In [90], a CNN-based automatic diagnosis method for prostate cancer images is proposed. Adopted the core concept of a CNN using multi-scale parallel branch, a multi-scale standard convolution method is developed. An architecture that combines the atrous spatial pyramid pooling from Deeplab-V3 and the network mentioned above as well as their feature maps are cascaded together to obtain initial segmentation results. Subsequently, a post-processing method that is based on CRF model is adopted to the prediction. The proposed system yielded an mIOU and overall pixel accuracy value of 0.773 and 0.895, respectively, for Gleason patterns segmentation.

In order to enhance the effectiveness of the network and solve the limitation of inconsistent data characteristics caused by random rotation in the learning process, a CNN based on a special convolution method and CRF is developed in [91]. This method uses the output probability of the CNN model to establish the unary potential

of FC-CRFs. And the feature map of adjacent patches is used to design a pair-wise loss function to represent the relationship between two blocks. The mean field approximate inference is applied to acquire the marginal distribution and calculate the cross entropy loss of the model. Thus, the whole network can be trained end-to-end. The experiment verifies that applying the CRFs can obviously improve the performance. Fig. 21 shows the comparison of the probability heat map of the cancer regions. And a segmentation accuracy and AUC of 85.1% and 91.0% are finally achieved on the test set.

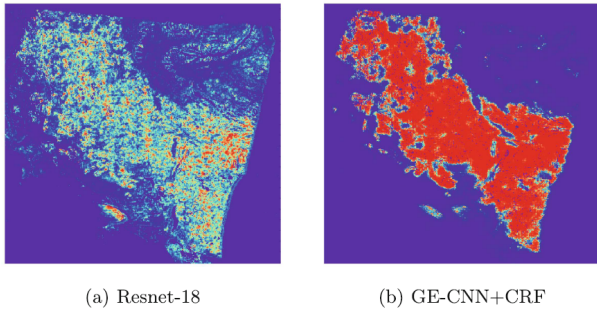


**Fig. 21** The probabilistic heat maps comparison between Resnet-18 and GE-CNN+CRF. This figure corresponds to Fig.7 in [91].

#### 4.2 Micro-alike Image Analysis

An intelligent semantic image analysis method is developed to detect cervical cancerous lesion based on colposcopy images in [92]. First, preprocessed images semantics maps are generated.  $k$ -means clustering is then applied to image segmentation. Thirdly, some distinguished features of cervical tissues are extracted. In the final step, a CRF-based method classifies the tissue in each region (segmented in the second step) as normal or abnormal. The CRF-based classifier combines the outputs of neighboring regions produced by  $k$ -NN and LDA classifier in a probabilistic manner. In the experiment of detecting neoplastic areas on colposcopic images obtained from 48 patients, an average sensitivity of 70% and a specificity of 80% are achieved. As an extension of this work, the performance evaluation step is improved in [93]. It is of great significance for the clinic to detect the abnormal area and provide a high-accuracy diagnosis. Considering this fact, a window-based method is proposed. The method first divides the image into patches, and then compares their classification results according to the ground truth in the histopathology images. In the same dataset, compared with expert colposcopy annotations (AUC=0.7177), the proposed

method gains better performance (AUC=0.8012). Fig. 22 presents examples of abnormal areas detected by proposed algorithm comparing the diagnostic accuracy with that of the colposcopist.

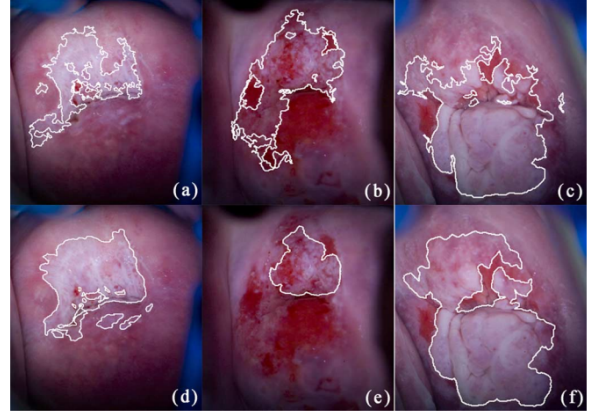


**Fig. 22** Acetowhite region detection by proposed algorithm. This figure corresponds to Fig.9 in [93].

In [94], a novel framework is presented for dividing vascular network into abnormal and normal areas from only taking the 3D structure of micro-vessel into consideration, where a distance map in preprocessed images is generated by computing the Euclidean distance first. Then, the inverse watershed of the distance map is computed. Finally, a CRF model is introduced to divide the watershed regions into tumor and non-tumor regions. Key images in the whole process are shown in Fig. 23. This method is tested in real intra-cortical images by Synchrotron tomography, which corresponds to the experts' expectation.

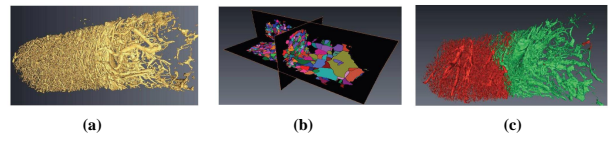


**Fig. 23** (a)Full data rendering after merging steps; (b) Watershed on the distance map; (c) The illustration of the segmentation result: the area in red represents normal tissue and green represents tumor. This figure corresponds to Fig.1,3,6 in original paper [94].

In [95], a method of fundus blood vessel segmentation based on discriminatively trained FC-CRF model is proposed. Unlike traditional CRF, in FC-CRF, each node is assumed to be each other's neighbors. Utilizing this method, not only the neighboring information can be considered, but also the relationship between distant pixels. Firstly, some features (Gabor wavelets, line detectors et al.) are extracted, serving as the parameters

of unary and pairwise energy combined with linear combination weight. Then, a supervised algorithm called Structured Output SVM is applied, which can learn the parameters for unary and pairwise potentials. On the DRIVE dataset, this method yields sensitivity 78.5%, specificity 96.7%. As an extension of this work, an intelligent method based on the similar workflow is introduced in [96] to overcome a limitation of previous research: the configuration of the pairwise potentials of the FC-CRF is affected by image resolution, because it is associated with the relative distance of each pixel. In order to solve this problem, an optimal parameter estimation method based on the feature parameters on a single data set is proposed, and it is multiplied by the compensation factor for adjustment. The authors manage to achieve over 96% accuracy and over 72% on DRIVE, STARE, HRF and CHASEDB1 four datasets.

In [97], for the objective of improving the accuracy of retinal vessel segmentation, a DL architecture is proposed. Fully CNNs are utilized for vessel probability map generation. Afterwards, an FC-CRF model is applied to build the long-range correlations between pixels to refine the segmentation result. Some of the unary and pairwise energy components are obtained by the vessel probability map. In the experiment, public dataset DRIVE and STARE achieve the segmentation accuracy of 94.70% and 95.45%. Furthermore, an improved system is introduced in [28]. A comprehensive deep network called DeepVessel is proposed, which consists of CNN stages and a CRF stage. A CNN integrating multi-scale and multi-level information with a delicately designed output layer to learn rich level representations is applied. The FC-CRF is applied in the last layer of the network, which is reformulated as an RNN layer so that it can be adopted in the end-to-end DL architecture. Its unary and pairwise terms are determined by the previous layers and its loss function is combined with the CNN layer loss function minimized by standard stochastic gradient descent. DeepVessel is tested in three public databases (DRIVE, STARE, and CHASE DB1), yielding an accuracy value of 95.23%, 95.85% and 94.89%, respectively. The results comparison is shown in Fig. 23.

A four-step method is developed for retinal vessel segmentation in [98]. Firstly, the image is preprocessed to remove noisy edges and normalized. Then, training a CNN to generate features that can be distinguished for the linear model. Third, in order to reduce the intensity difference between narrow blood vessels and wide blood vessels, a combined filter is used on the green channel to enhance the narrow blood vessels. Finally, the dense CRF model is applied to obtain the final segmentation of retinal blood vessels, whose unary potentials are

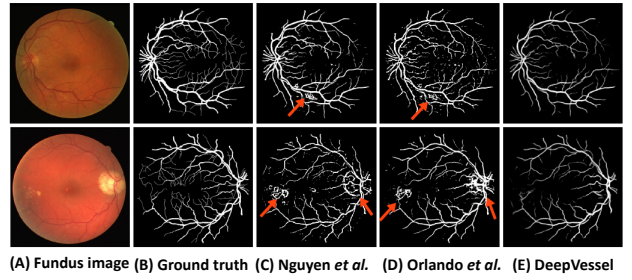


**Fig. 24** Retinal vessel segmentation results. This figure corresponds to Fig.1 in [28].

formulated by the discriminative features and pairwise potentials are comprised of the intensity value of pixel thin-vessel enhanced image. The work-flow of the whole process is shown in Fig. 25. Among DRIVE, STARE, CHASEDB1 and HRF four public dataset, proposed method achieves the best result in DRIVE (F1-score = 0.7942, Matthews correlation coefficient = 0.7656, G-mean = 0.8835).

An end-to-end algorithm is proposed in [99] for red and bright retinal lesions segmentation, which are essential biomarkers of DR. First, a patch-based multi-task learning framework is trained, which extends the function of U-Net. Then, CRF is used as the RNN to refine the segmentation output, and the rest of the network is applied to train the parameters of the kernel function. The softmax output of each decoding module in CNN is used as the unary potential. The binary potential is represented by the weighted sum of two Gaussian kernels. However, the results showed that the model performance deteriorated after adding the CRFs, because the CRFs add tiny false positive red lesions near blood vessels. This method is finally evaluated on a publicly available DIARETDB1 database and obtains specificity value of 99.8% and 99.9%, for red and bright retinal lesions detection respectively.

A novel approach combining the CNN with CRFD is proposed in [100] for purpose of detecting the optic disc in retinal image. CNN constructs the first-order potential function of CRF, and the second-order potential function is constructed by linear combination of Gaussian kernels. Lastly, in post-processing step, a regional restricts method is adopted to obtain the super-pixel area, which is used to make the connected area label consistent. Afterwards, in order to refine the results, the posterior probability mean of the super-pixel region is calculated. This method is verified on several retina databases and yields an accuracy of 100% in DRIVE, MESSID, DIARETDB, and DRION dataset. This method is improved and applied to other tasks like retina blood vessel segmentation and retina arteri-

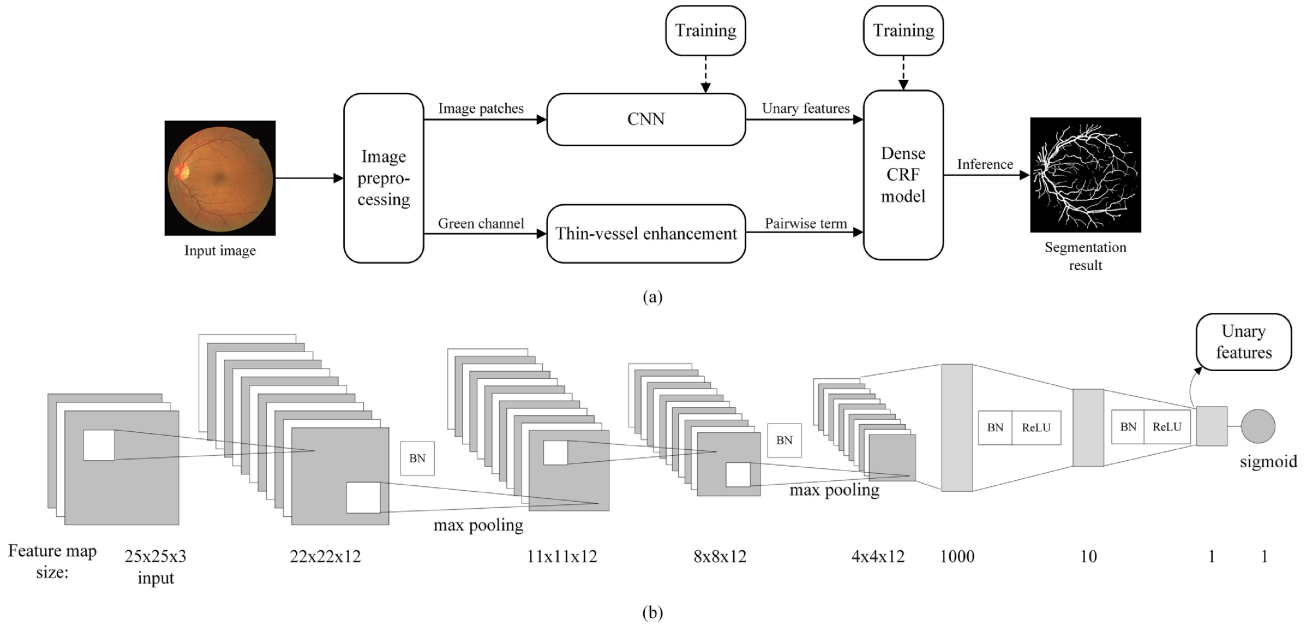


**Fig. 25** Overview of the retinal vessel segmentation method. (a) Work-flow of the proposed method. (b) The CNN's structure containing BN–Batch Normalization layer and ReLU–Rectified Linear Units applied for discriminative feature learning. This figure corresponds to Fig.1 in [98].

ovenous blood vessel classification in [101] by the same research team.

An automated optic disc segmentation method is proposed in [102]. The input image is trained by modified U-Net or DeepLabV3 network, and the prediction is resized and fed to the CRF for training and inference. However, the CRFs are not easily GPU accelerated leading to slower performance after added. Moreover, because of the smooth ground truth masks with little sharp deformation and the already satisfying boundary produced by neural networks, CRF has very little effect on performance improvement. No matter tested in private dataset or DRIONS-DB, RIM-ONE v.3, and DRISHTI-GS public dataset, Dice coefficient values all achieve over 95%.

A skin lesion segmentation ensemble learning framework on the basis of multiple deep convolutional neural network (DCNN) models are proposed in [103]. The whole process can be divided into three steps: First, in the training phase, multiple lesion segmentation maps are obtained from various pre-trained DCNN models, and then these segmentation maps are used as the unary potential of the CRF model. Lastly, the CRF energy is minimized and yields the final prediction. In the experiment, ISIC 2017 [104] and PH2 [105] public datasets are used for testing, and a mean Dice coefficient of 94.14% is finally achieved.

A novel framework for automatic auxiliary diagnosis of skin cancer is introduced [106]. The task of this framework is to segment and classify skin lesions. The

framework consists of two parts: The first part uses the encoder-decoder FCN to learn complex and uneven skin lesion features. Then the post-processing CRF module optimizes the output of the network. This module adopts the linear combination of Gaussian kernels as a binary potential for the objective of contour refinement and lesion boundary location. In the second part, the segmentation result is classified by the FCN-based DenseNet into 7 different categories. The classification accuracy, recall and AUC scores of 98%, 98.5%, and 99% are achieved on HAM10000 dataset of over 10000 images.

#### 4.3 Summary

A summary of the CRF methods for pathology image analysis is exhibited in Table 4., which contains some essential attributes of the summarized research papers. Each row indicates publication year, reference, research team, disease, input data, task, inference algorithm, classifier, result evaluation. Similar to the MRFs mentioned before, the CRFs is also widely applied to various diseases and mostly appears in segmentation and classification tasks. The mean-field approximation is the most common way to approximate maximum posterior marginal inference, and further explanation will be given in Section 5. Since 2016, DL network is applied on a wide range of computer vision tasks, including our research area especially related to the CRFs. Hence, features are rarely extracted in an independent step,

because the prepossessed image can be the input of DL method, which is more convenient. As shown from the chart, majority of the work achieves an accuracy of over 90%.

## 5 Method Analysis and Discussion

### 5.1 Analysis of MRF Methods

According to the researches on the MRF model applied in our field, it most frequently appears in segmentation task, and more specifically, plays two roles in most cases:

- It serves as a post-processing method to refine initial segmentation results obtained from classical segmentation methods;
- It is incorporated into other segmentation algorithms and they produce results together.

In the first case, the images are always segmented by some popular segmentation methods first to obtain initial labels, such as region growing,  $k$ -means, Bayesian classification, Otsu thresholding et al. However, most of these models do not consider contextual constraints, which have significant effect on the interpretation of visual information [107]. Therefore, the MRF is applied based on the initial label using spatial dependencies, producing the final labeling. Compared to the second situation, initial segmentation is helpful to avoid the MRF algorithm falling into local optimal solutions, but it makes the whole process more complex. The papers involved in this article are [50, 52, 55, 63, 64]. In the second case, the MRF is employed in the popular segmentation methods mentioned above, solving the limitation of those assumptions. Hence, random edges in the area due to noise are much less likely to cause false boundaries and better performance can be achieved. The papers involved in this article are [62, 69].

Parameter estimation and function optimization are essential to MRFs. Some algorithms are adopted for estimating observations from a given distribution. Among them, EM and ICM are the most widely used. The EM algorithm is an iterative algorithm for maximum likelihood estimation in the absence of data. Because of its simplicity and generality of the associated theory, it is broadly applicable these years [108]. However, compared to other algorithms, the convergence speed of the EM algorithm is relatively slow. The papers involved in this article are [50, 55, 62, 63].

Compared with the EM algorithm, ICM method not only guarantees the convergence of sequence update, but also has a higher speed, whose computation

time can be an order of magnitude less than other commonly used methods. The disadvantage is that different initial states lead to different results, which means that different MAP probabilities not always correspond to meaningful results. It seems to lack of mathematical justification. The papers involved in this article are [50, 54, 64, 66]. In [65], this algorithm is improved to adapt the task requirement, which adds a parameter to implicitly weight the importance of each class. The summary of the popular methods is shown in Fig. 26.

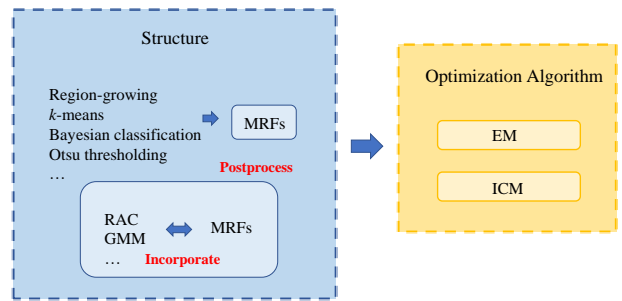


**Fig. 26** The popular methods in MRFs for pathology image analysis tasks.

### 5.2 Analysis of CRF Methods

Nowadays, various improvement measures have been proposed with the increasing influence of CRF. Among them, the FC-CRF which is also called dense CRF, is the most frequently employed discriminative model structure in the reviewed tasks, especially for the researches on eye diseases. Each node of the FC-CRF is a neighbor of each other. Therefore, contextual relationship of different types of labels or long-distance dependencies can be modeled to make the edges smoother and more coherent to semantic objects [7, 8]. The papers involved in this article are [28, 82, 84, 85, 87, 95–97] et al. The FC-CRF improves the accuracy, but increases computational cost. To circumvent the limitation, the mean-field approximation, a highly efficient approximate inference algorithm for FC-CRF, is proposed and become the most common inference approaches in the reviewed papers. The mean-field approximation algorithm is used to obtain the marginal label distribution of each patch, which is able to achieve significantly more accurate image-labeling performance and provide results in less than a second [109]. The papers involved in this article are [84, 87, 95, 97, 100].

Driven by the development of machine learning, from 2016, more and more researches integrate CRF into DL method, and they can be divided into two categories:

**Table 4** Summary of reviewed works for pathology image analysis using CRFs. (Matthews correlation coefficient (MCC), Free Response Receiver Operating Characteristic (FROC), intersection over union Coefficient (IoU), Aggregated Jaccard Index (AJI), mean intersection over union (mIOU), overall pixel accuracy (OPA), mean of accuracy (mAC), mean Dice Coefcient (mDC), mean Jaccard Index (mJI), mean thresholded Jaccard index (mTJI), mean Boundary Recall (mBR). )

Year, Ref, Research team	Disease	Input data	Task	Inference algori <th>thom</th> <th>Classifer</th> <th>Result evaluation</th>	thom	Classifer	Result evaluation
2009, [77], Wu et al.	–	FNA cytological samples from thyroid nodules, 12 images	Segmentation (cell or intercellular material)	Loopy belief propagation	–	–	–
2010, [92], Park et al.	Cervical cancer	Colposcopy images, 48 patients	Segmentation, classification (normal or abnormal)	–	KNN, LDA	Sn=70%, Sp=80%.	–
2011, [93], Park et al.	Cervical cancer	Colposcopy images, 48 patients	Segmentation, classification (normal or abnormal)	–	KNN, LDA	AUC=0.8012.	–
2011, [78], Rajapakse et al.	–	Lung tissue, 9551 cells	Classification (benign cells or cancer cells)	–	SVM	Acc=90.26%, Sn=48.30%, Sp=96.52%.	–
2011, [94], Descombes et al.	Brain tumor	Micro-tomography vascular networks	Segmentation of vascular networks (normal or tumor)	Simulated annealing	–	–	–
2012, [79], Fu et al.	–	Human colon tissues, 1072 glands	Gland detection and segmentation	Viterbi algorithm	SVR	Acc=70.32%.	–
2014, [80], Fu et al.	–	Human colon tissues, 1072 glands; 24 H&E stained images, 333 glands	Gland detection and segmentation	Viterbi algorithm	SVM, SVR	Dataset 1: Acc=80.4%; Dataset 2: Sn=82.35%, Sp=93.08%, Acc=87.02%, D=87.53%.	–
2014, [29], Manivan-nan et al.	Brain tumor	Brain tissue, 35 images	Region Segmentation (necrotic regions or normal regions)	Graph cuts	SVM (Bag-of-words)	Acc=66%.	–
2014, [95], Orlando et al.	Eye disease	Fundus retinal images, DRIVE public datasets	Retinal vessel segmentation	Mean-field inference	SOSVM	Sn=78.5%, Sp=96.7%.	–
2016, [81], Wang et al.	IBD	Intestinal tissue, 200 images	Semantic segmentation (muscle or messy regions)	–	FCN	Acc=90%, IU=56%.	–
2016, [97], Fu et al.	Eye disease	Fundus retinal images, DRIVE, STARE public datasets	Retinal vessel segmentation	Mean-field inference	CNN	DRIVE: Acc=94.70%, Sn=72.94%; STARE: Acc=95.45%, Sn=71.40%.	–
2016, [28], Fu et al.	Eye disease	Fundus retinal images, DRIVE, STARE, and CHASE DB1 public datasets	Retinal vessel segmentation	Stochastic gradient descent	CNN	DRIVE: Acc=95.23%, Sn=76.03%; STARE: Acc=95.85%, Sn=74.12%; CHASE DB1: Acc=94.89%, Sn=71.30%.	–
2016, [96], Orlando et al.	Eye disease	Fundus retinal images, DRIVE, STARE, CHASEDB1 and HRF public dataset	Retinal vessel segmentation	SOSVM	–	DRIVE: Sp=98.02%, Sn=78.97%; STARE: Sp=97.38%, Sn=76.92%; CHASE DB1: Sp=97.12%, Sn=72.77%; HRF: Sp=96.80%, Sn=78.74%.	–
2017, [98], Zhou et al.	Eye disease	Fundus retinal images, DRIVE, STARE, CHASEDB1 and HRF public dataset	Retinal vessel segmentation	Structured support vector machine, fast inference	Modified version of MatConvNet	DRIVE: F1-score= 0.7942, MCC=0.7656, G-mean=0.8835; STARE: F1-score=0.8017, MCC=0.7830, G-mean=0.8859; CHASEDB1: F1-score=0.7644, MCC=0.7398, G-mean=0.8579; HRF: F1-score=0.7627, MCC=0.7402, G-mean=0.8812.	–

Year, Ref, Research team	Disease	Input data	Task	Inference algorithom	Classfier	Result evaluation
2017, [82], Wu et al.	Breast cancer	Breast cancer biopsy images, 1136 images	Mitosis detection	Error back propagation	AlexNet	F=43.7%.
2017, [83], He et al.	—	Pluripotent stem cells, 306 sequences	Morphological change pattern classification (healthy, unhealthy or dying)	Margin maximization estimation	LCRF	Acc=93.46%.
2018, [84], Li et al.	Breast cancer	WSIs, 400 images	Classification (normal or tumor)	Mean-field inference	ResNet-18 and ResNet-34	FROC= 0.8096.
2018, [85], Liang et al.	Gastric cancer	Gastric tumor tissue, 1400 images	Segmentation (normal or tumor)	—	FCN	IoU=85.51%.
2018, [86], Liang et al.	Gastric cancer	Gastric tumor tissue, 1400 images	Segmentation (normal or tumor)	—	DU-Net	IoU=88.4%.
2018, [99], Playlout et al.	Diabetic retinopathy	Fundus retinal images, DIARETDB1 public dataset	Red and bright retinal lesions detection and segmentation	Adadelta algorithm	Modified version of U-Net	Red lesions: Sn= 66.9%, Sp=99.8%; bright lesions: Sn= 75.3%, Sp=99.9%.
2018, [100], Huang et al.	Eye disease	Fundus retinal images, DRIVE, STARE, MESSID, DIARETDB, DIARETD and DRION dataset	Optic disc identification	Mean-field inference	CNN	DRIVE, MESSID, DIARETDB, and DRION: Acc=100%; STARE: Acc=98.90%; DIARETD: Acc=99.90%.
2019, [87], Qu et al.	Lung Cancer	H&E stained histopathology images, lung cancer and MultiOrgan dataset	Nuclei segmentation	Mean-field inference	Modified version of U-net	Lung Cancer dataset: Acc=98.1%, F=92.6%, D=93.9%, AJI= 93.2%; MultiOrgan dataset: Acc=98.7%, F= 96%
2019, [88], Jamal et al.	—	Histopathological images, 58 images	Cellular segmentation	Iterated CRF	SVM, random forest, KNN	F=86.07%, Kappa=80.28%, Acc=91.79%.
2019, [89], Konstantinos et al.	Melanoma	Melanoma skin cancer, 105 images	Single-cell classification (cancer cells, lymphocytes, stromal cells or epidermal cells)	Stochastic gradient descent	SC-CNN	Acc=96.48%, P=96.44%, R=96.29%.
2020, [72] [74], Sun et al.	Gastric cancer	H&E stained gastric histopathological images, 560 images	Segmentation (normal or tumor)	—	CNNs	Acc=78.91%, P=41.58%, D=46.29%.
2020, [90], Li et al.	Prostate cancer	Prostate cancer tissue microarray, 1211 images	Gleason grading	—	ASPP and CNNs	mIOU=77.29%, OPA=89.51%.
2020, [102], Bhatkalkar et al.	Eye disease	Fundus retinal private dataset, 300 images	Segmentation of optic disc	—	DeepLabV3 et al.	DC=0.974.
2020, [103], Qiu et al.	Pigmented skin lesion	Dermoscopy images, ISIC 2017 and PH2 public dataset	Segmentation of skin lesion	Mean-field inference	DCNNs	mAC=96.20%, mDC=94.14%, mJI=89.20%, mTJI=68.10%.
2020, [106], Adegun et al.	Skin cancer	Dermatoscopic images, HAM10000 public dataset	Segmentation and classification of skin lesions	Mean-field inference	FCN-Based DenseNet framework	Acc=98.0%, F1-score=98.0%, R=98.5%.
2020, [91], Dong et al.	Prostate cancer	H&E stained WSIs of prostate tissue, 116 images	Segmentation (normal or tumor)	Mean-field inference	Resnet-GE-p4m	Acc=85.1%, AUC=91.0%.

- The DL network's outputs form the CRF components, and approximate maximum posterior marginal is inferred by optimization techniques afterwards (such as [72, 97, 98]);
- Firstly, approximate marginal distribution of each patch label is computed using the inference algorithm. Then, the CRFs are embedded in the loss function of DL network and they are trained together to minimize the loss and achieve optimal labels. (e.g. [28, 81, 84, 99], or the CRF loss is used to fine-tune the trained model, e.g. [82, 87]).

The former applies the CRFs as a post-processing step after DL network for purpose of incorporating contextual information. However, this does not fully harness the strength of CRFs since it is disconnected from the training of the DL network [110]. By contrast, the latter combines the DL network and CRF layers into an integrated DL architecture, which is an end-to-end learning method that reduces the complexity of the project. In [28, 81, 99], the CRFs are implemented as RNNs and embedded in the network as part of CNN, so the back propagation algorithm can be adopted to train the entire deep network end-to-end. The main advantages are as follows: First, DL network's lack of spatial and appearance consistency of the labelling output resulting in poor object delineation and classification accuracy loss. CRFs can be used to overcome this drawback, and this method combines the strengths of both of them. Second, although the DL network can provide a promising result, it has poor interpretability in mathematic theory [111]. However, the DL network and CRF are convertible. Therefore the CRF can be used to improve the interpretability of DL theory [110]. The CRFs have a solid theoretical foundation and can be converted into a DL network with good practical results. In conclusion, the CRFs have dual advantages in theory and practice, providing a unique perspective for pathology image analysis. The summary of the popular methods is shown in Fig. 27.

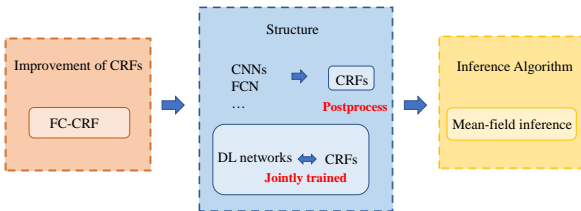


**Fig. 27** The popular methods in CRFs for pathology image analysis tasks.

### 5.3 The Potential Random Field Methods in Pathology Image Analysis Field

In this subsection, we will introduce some possible random field approaches, which have been applied to other types of image analysis tasks successfully. It can be speculated that they also have potential in pathological image analysis.

#### 5.3.1 Potential MRF Methods

With the continuous growth of the datasets, marking annotations associated with various groups of imaging functions and regions of interest is time-consuming and laborious. The max-flow algorithm is frequently applied in the MRF problems. In [112], an unsupervised method associated with the max-flow problem is proposed. An MRF prior is taken into consideration before the image's neighborhood structure, and then the flow capacities iteratively gain. Compared to other unsupervised methods, it is greatly improved and reaches more than 90% dice score in brain tumor MR images segmentation task. In [113], an approach focusing on solving a multi-atlas segmentation problem is proposed. The study reformulates the issue as a task of finding the optimal solution of MRF energy function. To optimize the objective MRF function, a max-flow-based optimization algorithm is introduced. This method is evaluated on the MR dataset, yielding mean Dice coefficients of nearly 90%.

The maximum flow technique can use reliable and efficient parallel algorithms for calculation and ensure its convergence, making it meet the requirement for large-scale tag optimization problems [113]. Especially in some whole slide image analysis tasks, it is hopeful that the MRFs with the Max-flow algorithm can handle this kind of work more efficiently.

#### 5.3.2 Potential CRF Methods

Recently, various improvements of the CRFs have been developed and applied in different domain [8]. The multi-label CRF is one of them, which is capable to mark one symbol with more than one label by using long-range interactions to encode contextual information. It can treat non-adjacent markers as one entity, and at the same time detect various types of objects in image segmentation tasks [114]. None of the previous researches applies the multi-label CRF for pathology image analysis tasks to the best of our knowledge.

A multi-label CRF for semantic image segmentation task is proposed in [114], where each layer stands for a single object class and is regularized independently. The

label space context is modeled by remote interactions between layers, where the sparse inter-layer connections penalize the unlikely occurrence of some groups of labels. They finally achieve state-of-the-art performance on the MSRC-1 and CorelB datasets. Moreover, in [115], a perturbation-based sampling approach for dense multi-label CRFs is introduced, which is computationally efficient and easy to implement. The method is validated on synthetic and clinical Magnetic Resonance Imaging data, achieving a promising result of the specificity value of 0.88 on the dataset containing 14 patients. Furthermore, an unmanned aerial vehicle (UAV) imagery classification problem is formulated within a multi-label CRF framework in [116]. Firstly, an appropriate representation and a classifier with multilayer are used to provide multi-label prediction probabilities in UAV image, which is segmented into patches. Second, the multi-label CRF model is applied to take spatial relationship between adjacent patches as well as labels within the same patch into consideration, aiming to improve the multi-label classification map iteratively. Outstanding performance achieves with 83.40% accuracy value.

In pathology image analysis field, most researches divide images into only two class, such as cancer versus non-cancer. However, the categories to be classified are not always antithetical. For example, in [117], the whole slide breast histopathology images can be labelled as five classes. So, it is believed that the multi-label CRF can show outstanding performance in the pathology image analysis field, especially in histopathology image and colposcopic image analysis.

Another improved model of the CRFs is the hierarchical CRF (HCRF) model, which belongs to the discriminative models and offers hierarchical and multi-level semantic. The HCRF model inherits the superiority of the CRF model, and achieve the combination of different scales of information [118] or the short-range as well as the long-range interactions [119]. Some notable applications of the HCRF for image classification problems are introduced below.

In [118], an HCRF model is proposed for radar image segmentation. The unary and pairwise potentials are constructed at each scale in order to integrate information in different scales. Besides, the mean-field approximation is employed to inference the best parameters for the HCRF model and maximize the posterior marginal estimation of the model. The proposed method yields a segmentation accuracy value of 89%. Similarly, an associative HCRF model is designed in [120] to improve the classification accuracy of high-resolution remote sensing images. The model is constructed on the graphics hierarchy. In this hierarchy, the pixel layer is

applied as the base layer, and multiple super-pixel layers are obtained by mean shift pre-segmentation. The proposed model's potentials are defined based on pixels' clustered features for super-pixels extracted at each layer. This method finally reaches an overall accuracy of 81.59%.

It has shown that learning discriminative patterns from the multiscale features delivers a more robust classifier with better discriminant performance in pathology image analysis task [121, 122]. It can be because of the way that the pathologists diagnose diseases, by examining macroscopical features to microcosmic features. These arguments demonstrate the HCRF method's potential, which can be applied in our field, especially in histopathology image analysis.

#### 5.4 The Random Field Methods for Other Potential Fields

The MRF and CRF methodology discussed in this paper not only can be applied in pathology image analysis domain but also can perform well in other fields, such as remote sensing images, computed tomography images, magnetic resonance imaging, and images collected by pipe robots. There are many intelligent diagnosis systems developed for high-resolution remote sensing image segmentation [123, 124]. The remote sensing images share the same rotating properties with cytopathology images, which are both without directivity. For example, SuperCRF in [89] models cells and super-pixels as nodes as well as edges between the nodes if there is a contextual connection among nodes by a CRF. Thus, it is highly possible to apply for remote sensing image segmentation. Besides, the discussed segmentation algorithms also have potential applications in CT and MRI. In microaneurysms (MAs) detection tasks, there are two difficulties: nonuniformity of background intensity and the unequal amount of background pixels and MAs. Thrombus [125, 126] and pulmonary nodule [127] detection tasks also have these characteristics. Moreover, the thrombus geometric structure is irregular, which is similar to that of the optic disk. Thus, the MRF applied in [59] has a possibility to employ in these two fields. The instability of light in tunnels and the camera's angle and distance from the surface are two serious problems when detecting images captured by pipe robot. Meanwhile, the endoscopic image analysis also meets this question [128, 129]. So, the CRF model proposed in [92, 93] can find significant use in this area. In conclusion, MRF and CRF methods summarized in this survey can offer a new perspective to the research in other domains.

## 6 Conclusion

The MRFs and CRFs have attracted significant attention from researchers in various research fields since being proposed. This paper reviews the recent study about the MRF and CRF models applied in pathology image analysis. First, this review presents an introduction to random field models and pathology. Second, it elaborates on both models' background knowledge, including their property, modelling, and inference processes. Thirdly, the research papers of random fields based pathology image analysis are comprehensively summarized and some prevalent methods are discussed, which are grouped according to their tasks and categories of images, respectively. Finally, the conclusion are given in this section. The review shows that pathology image analysis using the MRFs and CRFs is an increasing topic of interest and improves the performance. Besides, they are believed to be applicable to a wider range of research fields to better solve some problems in the future.

**Acknowledgements** This work is supported by the “National Natural Science Foundation of China” (No. 61806047), the “Fundamental Research Funds for the Central Universities” (No. N2019003) and the “China Scholarship Council” (No. 2018GBJ001757). We thank Miss Zixian Li and Mr. Guoxian Li for their important support and discussion in this work.

## References

1. U. Grenander, Brown University, Division of Applied Mathematics (1983)
2. J.P. Monaco, A. Madabhushi, Medical Image Analysis **16**(8), 1477 (2012)
3. J. Besag, Journal of the Royal Statistical Society: Series B (Methodological) **36**(2), 192 (1974)
4. S.Z.Li, *Markov Random Field Modeling in Computer Vision* (Springer, Japan, 1995)
5. Y. Zhang, M. Brady, S. Smith, IEEE Transactions on Medical Imaging **20**(1), 45 (2001)
6. Q. Wang, arXiv preprint arXiv:1212.4527 (2012)
7. S. Wu, X. Weng, arXiv preprint arXiv:1811.11323 (2018)
8. B. Yu, Z. Fan, Artificial Intelligence Review pp. 1–45 (2019)
9. A. McCallum, D. Freitag, F.C. Pereira, in *ICML* (2000), pp. 591–598
10. L. Rabiner, B. Juang, IEEE assp magazine **3**(1), 4 (1986)
11. J. Lafferty, A. McCallum, F.C. Pereira, (2001)
12. X. Zhang, Y. Jiang, H. Peng, K. Tu, D. Goldwasser, in *Proceedings of the 2017 Conference on Empirical Methods in Natural Language Processing* (2017), pp. 1701–1711
13. A.F. Wicaksono, S.H. Myaeng, in *Proceedings of the 22nd ACM International Conference on Information & Knowledge Management* (2013), pp. 2039–2048
14. L. Zhuowen, K. Wang, in *2013 25th Chinese Control and Decision Conference (CCDC)* (2013), pp. 1506–1510
15. S.S. Kruthiventi, R.V. Babu, in *2015 IEEE International Conference on Image Processing (ICIP)* (2015), pp. 3417–3421
16. D.Y. Liliana, C. Basaruddin, in *2017 International Conference on Electrical Engineering and Computer Science (ICECOS)* (2017), pp. 143–148
17. L.C. Chen, G. Papandreou, I. Kokkinos, K. Murphy, A.L. Yuille, arXiv preprint arXiv:1412.7062 (2014)
18. World-Health-Organization, *Guide for Establishing a Pathology Laboratory in the Context of Cancer Control* (World Health Organization, US, 2019)
19. World-Health-Organization, *Guide To Cancer Early Diagnosis* (World Health Organization, US, 2017)
20. World-Health-Organization. Early cancer diagnosis saves lives, cuts treatment costs. <https://www.who.int/news-room/detail/03-02-2017-early-cancer-diagnosis-saves-lives-cuts-treatment-costs> (2017)
21. World-Health-Organization. Cancer Diagnosis and Treatment. <https://www.who.int/cancer/treatment/en/> (2020)
22. A. Janowczyk, A. Madabhushi, Journal of Pathology Informatics **7**(1), 29 (2016)
23. T.J. Fuchs, J.M. Buhmann, Computerized Medical Imaging and Graphics **35**(7-8), 515 (2011)
24. B. Kong, X. Wang, Z. Li, Q. Song, S. Zhang, in *International Conference on Information Processing in Medical Imaging* (2017), pp. 236–248
25. S. Doyle, S. Agner, A. Madabhushi, M. Feldman, J. Tomaszewski, in *2008 5th IEEE International Symposium on Biomedical Imaging: From Nano to Macro* (2008), pp. 496–499
26. F.G. Zanjani, S. Zinger, et al., in *Medical Imaging 2018: Digital Pathology* (2018), p. 105810I
27. A. Arnab, S. Zheng, S. Jayasumana, B. Romera-Paredes, M. Larsson, A. Kirillov, B. Savchynskyy, C. Rother, F. Kahl, P.H. Torr, IEEE Signal Processing Magazine **35**(1), 37 (2018)
28. H. Fu, Y. Xu, S. Lin, D.W.K. Wong, J. Liu, in *International Conference on Medical Image Computing and Computer-assisted Intervention* (2016), pp. 132–139
29. S. Manivannan, H. Shen, W. Li, R. Annunziata, H. Hamad, R. Wang, J. Zhang, Technique Report (2014)
30. C. Wang, N. Komodakis, N. Paragios, Computer Vision and Image Understanding **117**(11), 1610 (2013)
31. H.Y. Chang, C.K. Jung, J.I. Woo, S. Lee, J. Cho, S.W. Kim, T.Y. Kwak, Journal of Pathology and Translational Medicine **53**(1), 1 (2019)
32. C. Li, H. Chen, X. Li, N. Xu, Z. Hu, D. Xue, S. Qi, H. Ma, L. Zhang, H. Sun, Artificial Intelligence Review pp. 1–42 (2020)
33. G. Litjens, T. Kooi, B.E. Bejnordi, a.a.a. Setio, F. Ciompi, M. Ghafoorian, J.a. Van Der Laak, B. Van Ginneken, C.I. Sánchez, Medical Image Analysis **42**, 60 (2017)
34. S. Wang, D.M. Yang, R. Rong, X. Zhan, G. Xiao, The American Journal of Pathology (2019)
35. M.M. Rahaman, C. Li, X. Wu, Y. Yao, Z. Hu, T. Jiang, X. Li, S. Qi, IEEE Access **8**, 61687 (2020)
36. L. He, L.R. Long, S. Antani, G.R. Thoma, Computer Methods and Programs in Biomedicine **107**(3), 538 (2012)
37. F. Xing, L. Yang, IEEE Reviews in Biomedical Engineering **9**, 234 (2016)

38. H. Irshad, A. Veillard, L. Roux, D. Racoceanu, *IEEE Reviews in Biomedical Engineering* **7**, 97 (2013)

39. L. He, L.R. Long, S. Antani, G. Thoma, *Sequence and Genome Analysis: Methods and Applications* **3**, 271 (2010)

40. D. Komura, S. Ishikawa, *Computational and Structural Biotechnology Journal* **16**, 34 (2018)

41. J. Staal, M.D. Abramoff, M. Niemeijer, M. a. Viergever, B. van Ginneken, *IEEE Transactions on Medical Imaging* **23**(4), 501 (2004)

42. A.D. Hoover, V. Kouznetsova, M. Goldbaum, *IEEE Transactions on Medical Imaging* **19**(3), 203 (2000)

43. C.G. Owen, a.R. Rudnicka, R. Mullen, S.a. Barman, D. Monekosso, P.H. Whincup, J. Ng, C. Paterson, *Investigative Ophthalmology & Visual Science* **50**(5), 2004 (2009)

44. J. Odstrcilik, R. Kolar, a. Budai, J. Hornegger, J. Jan, J. Gazarek, T. Kubena, P. Cernosek, O. Svoboda, E. Angelopoulou, *IET Image Processing* **7**(4), 373 (2013)

45. E.J. Carmona, M. Rincón, J. García-Feijoó, J.M. Martínez-de-la Casa, *Artificial Intelligence in Medicine* **43**(3), 243 (2008)

46. E. Decencière, X. Zhang, G. Cazuguel, B. Lay, B. Cochener, C. Trone, P. Gain, R. Ordonez, P. Massin, A. Erginay, B. Charton, J.C. Klein, *Image Analysis & Stereology* **33**(3), 231 (2014)

47. J. Monaco, J.E. Tomaszewski, M.D. Feldman, M. Moradi, P. Mousavi, A. Boag, C. Davidson, P. Abolmaesumi, A. Madabhushi, in *Medical Imaging 2009: Image Processing* (2009), p. 725903

48. J. Xu, J.P. Monaco, R.E. Sparks, A. Madabhushi, *Journal of Medical Imaging* **4**(2), 021107 (2017)

49. X. Wu, V. Kumar, J.R. Quinlan, J. Ghosh, Q. Yang, H. Motoda, G.J. McLachlan, A. Ng, B. Liu, S.Y. Philip, et al., *Knowledge and Information Systems* **14**(1), 1 (2008)

50. T. Mungle, S. Tewary, D. Das, I. arun, B. Basak, S. agarwal, R. ahmed, S. Chatterjee, C. Chakraborty, *Journal of microscopy* **267**(2), 117 (2017)

51. V. Meas-Yedid, S. Tilie, J.C. Olivo-Marin, in *Object recognition supported by user Interaction for service robots* (2002), pp. 796–799

52. C.S. Won, J.Y. Nam, Y. Choe, in *Computer Vision and Mathematical Methods in Medical and Biomedical Image Analysis* (Springer, 2004), pp. 281–291

53. G. Zou, J. Sun, Y. Ao, *Computer Engineering and Design* **030**(22), 5155 (2009)

54. A.N. Basavanhally, S. Ganesan, S. Agner, J.P. Monaco, M.D. Feldman, J.E. Tomaszewski, G. Bhanot, A. Madabhushi, *IEEE Transactions on Biomedical Engineering* **57**(3), 642 (2009)

55. J. Bioucas-Dias, F. Condessa, J. Kovačević, in *Image Processing: Algorithms and Systems XII* (2014), p. 90190P

56. A. Salazar-Gonzalez, D. Kaba, Y. Li, X. Liu, *IEEE Journal of Biomedical Health Informatics* **18**(6), 1874 (2014)

57. Z. Liu, *Study on Algorithm for Melanoma Recognition based on Dermoscopy*. Ph.D. thesis, University of Electronic Science and Technology of China (2015)

58. M. Paramanandam, M. O'Byrne, B. Ghosh, J.J. Mammen, M.t. Manipadam, R. Thamburaj, V. Pakrashi, *PloS one* **11**(9), e0162053 (2016)

59. R. Ganjee, R. Azmi, M.E. Moghadam, *Journal of Medical Systems* **40**(3), 74 (2016)

60. L. Zhao, K. Li, M. Wang, J. Yin, E. Zhu, C. Wu, S. Wang, C. Zhu, *Computers in Biology and Medicine* **71**, 46 (2016)

61. A. GençTav, S. Aksoy, S. ÖNder, *Pattern Recognition* **45**(12), 4151 (2012)

62. M. Dholey, M. Maity, A. Sarkar, A. Giri, A. Sadhu, K. Chaudhury, S. Das, J. Chatterjee, in *Advanced Computational and Communication Paradigms* (2018), pp. 695–705

63. J. Su, S. Liu, *Journal of Harbin Engineering University* pp. 400–405 (2019)

64. J. Monaco, J. Tomaszewski, M. Feldman, M. Moradi, P. Mousavi, A. Boag, C. Davidson, P. Abolmaesumi, A. Madabhushi, in *Workshop on Microscopic Image Analysis with Applications in Biology (in conjunction with MICCAI)* (2008)

65. J. Monaco, S. Viswanath, A. Madabhushi, Program Committee John Ashburner (University College London) Sylvain Bouix (Harvard Medical School) Tim Cootes (University of Manchester) **209** (2009)

66. J.P. Monaco, J.E. Tomaszewski, M.D. Feldman, I. Hagemann, M. Moradi, P. Mousavi, A. Boag, C. Davidson, P. Abolmaesumi, A. Madabhushi, *Medical Image Analysis* **14**(4), 617 (2010)

67. J.P. Monaco, A. Madabhushi, *IEEE Transactions on Medical Imaging* **30**(7), 1353 (2011)

68. E. Yu, J.P. Monaco, J. Tomaszewski, N. Shih, M. Feldman, A. Madabhushi, in *2011 Annual International Conference of the IEEE Engineering in Medicine and Biology Society* (2011), pp. 3427–3430

69. J. Xu, J.P. Monaco, A. Madabhushi, in *International Conference on Medical Image Computing and Computer-Assisted Intervention* (2010), pp. 197–204

70. J. Xu, J.P. Monaco, R. Sparks, A. Madabhushi, *Journal of Medical Imaging* **4**(2), 021107 (2017)

71. O.S. Al-Kadi, *Pattern recognition* **43**(6), 2043 (2010)

72. C. Sun, C. Li, J. Zhang, F. Kulwa, X. Li, *Electronics Letters* **56**, 750 (2020)

73. E. Letters, *Electronics Letters* **56**(15), 747 (2020)

74. C. Sun, C. Li, J. Zhang, M.M. Rahaman, S. Ai, H. Chen, F. Kulwa, Y. Li, X. Li, T. Jiang, *Biocybernetics and Biomedical Engineering* **40**(40), 1535 (2020)

75. S. Rachel, A. Madabhushi, *Medical Image Analysis* **17**(8), 997 (2013)

76. World-Health-Organization. An Introduction to Colposcopy: Indications for Colposcopy, instrumentation, Principles and Documentation of Results. <https://screening.iarc.fr/colpochap.php?lang=1&chap=4>

77. X. Wu, S.K. Shah, in *Workshop on Optical Tissue Image Analysis in Microscopy, Histopathology and Endoscopy (in conjunction with MICCAI)* (2009)

78. J.C. Rajapakse, S. Liu, in *2011 Annual International Conference of the IEEE Engineering in Medicine and Biology Society* (2011), pp. 5128–5131

79. H. Fu, G. Qiu, M. Ilyas, J. Shu, in *British Machine Vision Conference* (2012), pp. 1–12

80. H. Fu, G. Qiu, J. Shu, M. Ilyas, *IEEE Transactions on Medical Imaging* **33**(3), 764 (2014)

81. J. Wang, J.D. MacKenzie, R. Ramachandran, D.Z. Chen, in *International Conference on Medical Image Computing and Computer-Assisted Intervention* (2016), pp. 176–184

82. B. Wu, *Mitosis Detection in Breast Cancer Based on Convolutional Neural Network*. Ph.D. thesis, Harbin Institute of Technology (2017)

83. F. He, *Reasearch of Key Technologies for Microcell Image Sequence Morphology Analysis*. Ph.D. thesis, Southeast University (2017)

84. Y. Li, W. Ping, *Computing Research Repository (CoRR)* **abs/1806.07064** (2018)

85. Q. Liang, Y. Nan, G. Coppola, K. Zou, W. Sun, D. Zhang, Y. Wang, G. Yu, *IEEE Journal of biomedical and health informatics* **23**(3), 1205 (2018)

86. Q. Liang, Y. Nan, S. Xiang, I. Mei, W. Sun, G. Yu,

87. H. Qu, P. Wu, Q. Huang, J. Yi, G.M. Riedlinger, S. De, D.N. Metaxas, in *International Conference on Medical Imaging with Deep Learning* (2019), pp. 390–400

88. S.B. Jamal, *IEEE TSP2019* (2019)

89. Z.P. Konstantinos, F. Henrik, R. SEA, R. Ioannis, J. Yann, Y. Yinyin, *Frontiers in Oncology* (2019)

90. Y. Li, M. Huang, Y. Zhang, J. Chen, H. Xu, G. Wang, W. Feng, *IEEE Access* **8**, 117714 (2020)

91. J. Dong, X. Guo, G. Wang, in *Proceedings of 2020 Chinese Intelligent Systems Conference* (Springer Singapore, 2021), pp. 646–658

92. S.Y. Park, D. Sargent, R. Wolters, R.W. Lieberman, in *2010 IEEE Fourth International Conference on Semantic Computing* (2010), pp. 160–165

93. S.Y. Park, D. Sargent, R. Lieberman, U. Gustafsson, *IEEE Transactions on Medical Imaging* **30**(3), 867 (2011)

94. X. Descombes, F. Plouraboué, A. Boustanli, C. Fonta, G. LeDuc, R. Serduc, T. Weitkamp, in *Proceedings - International Symposium on Biomedical Imaging* (2011), pp. 1113–1116

95. J.I. Orlando, M. Blaschko, in *International Conference on Medical Image Computing and Computer-Assisted Intervention* (2014), pp. 634–641

96. J. Orlando, E. Prokofyeva, M. Blaschko, *IEEE Transactions on Biomedical Engineering* **64**, 16 (2016)

97. H. Fu, Y. Xu, D. Wong, J. Liu, in *2016 IEEE 13th International Symposium on Biomedical Imaging (ISBI)* (2016), pp. 698–701

98. L. Zhou, Q. Yu, X. Xu, Y. Gu, J. Yang, *Computer methods and Programs in Biomedicine* **148**, 13 (2017)

99. C. Playout, R. Duval, F. Cheriet, in *International Conference on Medical Image Computing and Computer-Assisted Intervention* (2018), pp. 101–108

100. W. Huang, D. Wen, M. Dewan, Y. Yan, K. Wang, in *2018 IEEE SmartWorld, Ubiquitous Intelligence & Computing, Advanced & Trusted Computing, Scalable Computing & Communications, Cloud & Big Data Computing, Internet of People and Smart City Innovation (SmartWorld/SCALCOM/UIC/ATC/CBDCom/IOP/SCI)* (2018), pp. 1917–1922

101. W. Huang, Research on Detection Methods of Related Targets in Color Fundus Retina Image. Ph.D. thesis, Jilin University (2018)

102. B.J. Bhatkalkar, D.R. Reddy, S. Prabhu, S.V. Bhandary, *IEEE Access* **8**, 29299 (2020)

103. Y. Qiu, J. Cai, X. Qin, J. Zhang, *IEEE Access* **8**, 144246 (2020)

104. N.C. Codella, D. Gutman, M.E. Celebi, B. Helba, M.A. Marchetti, S.W. Dusza, A. Kalloo, K. Liopyris, N. Mishra, H. Kittler, et al., in *2018 IEEE 15th International Symposium on Biomedical Imaging (ISBI 2018)* (2018), pp. 168–172

105. T. Mendonça, P.M. Ferreira, J.S. Marques, Marcal, ré RS, J. Rozeira, in *2013 35th Annual International Conference of the IEEE Engineering in Medicine and Biology Society (EMBC)* (2013), pp. 5437–5440

106. A.A. Adegun, S. Viriri, *IEEE Access* **8**, 150377 (2020)

107. S.Z. Li, *Markov Random Field Modeling in Image Analysis* (Springer Science & Business Media, 2009)

108. A.P. Dempster, N.M. Laird, D.B. Rubin, *Journal of the Royal Statistical Society: Series B (Methodological)* **39**(1), 1 (1977)

109. P. Krähenbühl, V. Koltun, in *Advances in Neural Information Processing Systems* (2011), pp. 109–117

110. S. Zheng, S. Jayasumana, B. Romera-Paredes, V. Vineet, Z. Su, D. Du, C. Huang, P.H. Torr, in *Proceedings of the IEEE International Conference on Computer Vision* (2015), pp. 1529–1537

111. Y. LeCun, in *IEEE Conference on Computer Vision and Pattern Recognition* (2015)

112. A.S. Iquebal, S. Bukkapatnam. Unsupervised Image Segmentation via Maximum a Posteriori Estimation of Continuous Max-Flow. <https://deepai.org/publication/unsupervised-image-segmentation-via-maximum-a-posteriori-estimation-of-continuous-max-flow> (2018)

113. L.M. Koch, M. Rajchl, W. Bai, C.F. Baumgartner, T. Tong, J. Passerat-Palmbach, P. Aljabar, D. Rueckert, *IEEE Transactions on Pattern Analysis and Machine Intelligence* **40**(7), 1683 (2017)

114. C. Wei, X. Jiang, Z. Tang, W. Qian, N. Fan, *Artificial Intelligence Review* **43**(4), 579 (2015)

115. R. Meier, U. Knecht, A. Jungo, R. Wiest, M. Reyes, Computing Research Repository (CoRR) [abs/1703.00312](https://arxiv.org/abs/1703.00312) (2017)

116. A. Zeggada, S. Benbraika, F. Melgani, Z. Mokhtari, *IEEE Geoscience and Remote Sensing Letters* **15**(3), 399 (2018)

117. C. Mercan, S. Aksoy, E. Mercan, L.G. Shapiro, D.L. Weaver, J.G. Elmore, *IEEE Transactions on Medical Imaging* **37**(1), 316 (2017)

118. P. Zhang, M. Li, Y. Wu, H. Li, *IEEE Transactions on Geoscience and Remote Sensing* **53**(9), 4933 (2015)

119. S. Kumar, M. Hebert, in *Tenth IEEE International Conference on Computer Vision (ICCV'05) Volume 1* (2005), pp. 1284–1291

120. Y. Yang, A. Stein, V.A. Tolpekin, Y. Zhang, *IEEE Geoscience and Remote Sensing Letters* **15**(5), 754 (2018)

121. M.S. Jain, T.F. Massoud, *Nature Machine Intelligence* **2**(6), 356 (2020)

122. Z. Ning, X. Zhang, C. Tu, Q. Feng, Y. Zhang, *IEEE Access* **7**, 150910 (2019)

123. M. Wang, Z. Dong, Y. Cheng, D. Li, *IEEE Transactions on Geoscience and Remote Sensing* **56**(1), 228 (2017)

124. Troya-Galvis, rés, P. Gançarski, L. Berti-Équille, *Pattern Recognition* **73**, 259 (2018)

125. J. Takasugi, H. Yamagami, T. Noguchi, Y. Morita, T. Tanaka, Y. Okuno, S. Yasuda, K. Toyoda, Y. Gon, K. Todo, et al., *Stroke* **48**(9), 2434 (2017)

126. K. López-Linares, N. Aranjuelo, L. Kabongo, G. Maclair, N. Lete, M. Ceresa, A. García-Familiar, I. Macía, M.a.G. Ballester, *Medical Image Analysis* **46**, 202 (2018)

127. T. Messay, R.C. Hardie, S.K. Rogers, *Medical Image Analysis* **14**(3), 390 (2010)

128. K. Loupos, A.D. Doulamis, C. Stentoumis, E. Protopapadakis, K. Makantasis, N.D. Doulamis, A. Amditis, P. Chrobocinski, J. Victores, R. Montero, et al., *International Journal of Intelligent Robotics and Applications* **2**(1), 43 (2018)

129. H. Huang, Q. Li, D. Zhang, *Tunnelling and Underground Space Technology* **77**, 166 (2018)